## Master's Degree in Aerospace Engineering



## Politecnico di Torino

Hybrid Low-Thrust and Chemical Propulsion for Optimal Mars Landing Trajectories via the Indirect Method

Supervisors:
Manuela Battipede
Luigi Mascolo

Candidate:
Achille Di Lauro

## Acknowledgements

I would like to thank Prof. Manuela Battipede for giving me the opportunity to write this thesis and for instilling in me, through her lessons, a curiosity and desire to learn about astrodynamics.

My sincere thanks also go to Dr. Luigi Mascolo for his constant support, valuable teachings and advice throughout the thesis. His availability and presence during this journey were fundamental to the completion of this work.

Turin, October 2025 Achille

## Abstract

The exploration of Mars represents one of the most ambitious missions for the conquest of space. It is not just a question of pushing man into territories never before physically reached, but also of deepening scientific knowledge through the search for possible forms of past microbial life and the analysis of rocks and craters, comparing them with those on Earth. Furthermore, a possible future colonisation of the red planet would open up significant economic scenarios linked to the exploitation of new resources and the development of advanced technologies.

This thesis aims to study and optimise trajectory control during the landing phase on Mars. Trajectory optimisation is carried out using the indirect method. This approach transforms the problem of maximising the final mass into a Multi-Point Boundary Value Problem (MPBVP), solved through a multi-shooting iterative procedure based on Pontryagin's Maximum Principle (PMP). In order to minimise propellant consumption and maximise payload, a hybrid propulsion configuration was adopted, consisting of an electric motor and a chemical motor: the former used in the initial phases to maximise energy efficiency, and the latter in the terminal phase to ensure a controlled and precise landing.

The dynamic method adopted includes a two-body model, in which atmospheric resistance is considered as a perturbative effect. Atmospheric density data were calculated using NASA's Mars Global Reference Atmospheric Model (Mars-GRAM) software, which allows the density value to be evaluated as altitude, latitude and longitude vary. The optimal descent trajectory is sought by imposing boundary conditions and internal conditions that allow the orbit to be gradually reduced. This optimisation is carried out considering both variable-time and fixed-time scenarios.

## Table of Contents

Li	st of	Tables	VII
Li	$\operatorname{st}$ of	Figures	/III
A	crony	vms	X
1	Intr	roduction	1
	1.1	Preface	1
	1.2	Optimization for Spacecraft Trajectories	2
	1.3	Overview of Chapters	4
2	Dyr	namic Model	6
	2.1	Newton's Gravitational Law	7
	2.2	N-Body Problem	7
		2.2.1 Absolute motion	7
		2.2.2 Relative motion	10
	2.3	Two Body Problem	10
		2.3.1 Equation of motion	11
		2.3.2 Polar equation of a conic section	13
	2.4	Reference System	16
		2.4.1 Orbital parameters	17
		2.4.2 Equation of motion in spherical coordinates	19
	2.5	Perturbing Forces	23
		2.5.1 Atmospheric drag	25
		2.5.2 Mars asphericity	26
		2.5.3 Third-body perturbations	27
		2.5.4 Solar radiation	29
3	Atn	nospheric Density	31
	3.1	Modelling of Martian Atmospheric Density	31
	3.2	Use of the Mars-GRAM Model for Atmospheric Analysis	33

		1			
	3.3	Analysis of the Case Study Results			
		3.3.1 Preparation and compilation of Mars-GRAM	37		
		3.3.2 Trend of atmospheric density as a function of spatial coordinates	38		
4	Opt	imal Control Problem	44		
	4.1	Difference Between Direct and Indirect Numerical Methods	45		
	4.2	Optimal Control Problem	45		
		4.2.1 Boundary conditions for optimality	47		
		4.2.2 Adjoint and control variables	48		
	4.3	Multi-Point Optimal Control Problem	49		
	4.4	Differential Correction	50		
		4.4.1 Single shooting	53		
		4.4.2 Multiple shooting	55		
		4.4.3 Variable-time vs fixed-time	55		
	4.5	Application of OCP to the Case Study	56		
5	Res	ults	59		
	5.1	Ion Thrusters	61		
	5.2	Parachute	68		
	5.3	Chemical Thrusters	69		
	5.4	Overview	71		
6	Con	clusions	74		
	6.1	Key strengths	74		
	6.2	Limitations	74		
	6.3	Next Steps in the Research	75		
$\mathbf{A}$	Rot	ational Matrices	76		
В	$\mathbf{Sph}$	erical Unit Vectors	77		
$\mathbf{C}$	Eule	er-Lagrange equations for the adjoint variables	78		
Bi	hliog	raphy	Rihliography 79		

## List of Tables

2.1	Classification of conic sections based on $\mathscr{E}$ , $a, e \ldots \ldots \ldots$	14	
2.2	Cosmic velocities of the Earth	16	
2.3	Definition of the six classical orbital elements	19	
2.4	Comparison between gravitational and perturbative accelerations .	29	
3.1	Mars gravity parameters	35	
5.1	Initial state for the first manoeuvre	61	
5.2	Initial conditions of the adjoint variables for the first manoeuvre,		
	including switching and final time	61	
5.3	Boundary conditions for the first manoeuvre	62	
5.4	Final state for the first manoeuvre	62	
5.5	Error on the BCs for the first manoeuvre	63	
5.6	Initial state for the second manoeuvre	63	
5.7			
	including switching and final time	64	
5.8	Boundary conditions for the second manoeuvre	64	
5.9	Error on the BCs for the second manoeuvre	65	
5.10	Final state for the second manoeuvre	65	
5.11	Initial state for the third manoeuvre	66	
5.12	Initial conditions of the adjoint variables for the third manoeuvre,		
	including switching and final time	66	
	Boundary conditions for the third manoeuvre	67	
	Final state for the third manoeuvre	67	
5.15	Error on the BCs for the third manoeuvre	67	
5.16	Initial state for the trajectory with parachute	68	
5.17	Initial state for the last manoeuvre	69	
5.18	Initial conditions of the adjoint variables for the last manoeuvre,		
	including switching and final time	70	
5.19	Boundary conditions for the last manoeuvre	70	
5.20	Final state	71	

# List of Figures

2.1	Gravitational interaction between two point masses	8
2.2	Gravitational interactions in an N-body system	9
2.3	Gravitational interactions in a two body system	11
2.4	Assessment of the Sphere of Influence	15
2.5	Mars RS $(\hat{I}, \hat{J}, \hat{K})$	17
2.6	Orbital parameters	18
2.7	Perifocal RS	20
2.8	Representation of the position vector in spherical coordinates within	
	the Mars-centred equatorial inertial RS	21
2.9	Evolution of the orbital inclination over time: comparison between	
	the Keplerian case and the perturbative effects	24
2.10	Third-body interaction scheme	27
3.1	Example of an Output file generated by Mars-GRAM	32
3.2	Cube for trilinear interpolation	33
3.3	Output BLDTRAJ.f90	38
3.4	Input file Mars-GRAM	39
3.5	Mars-GRAM running	39
3.6	Atmospheric density profiles on Mars at altitude = 10 km	40
3.7	Atmospheric density profiles on Mars at latitude = $0^{\circ}$	41
3.8	Atmospheric density profiles on Mars at longitude = $0^{\circ}$	42
3.9	Atmospheric density profiles on Mars at longitude = $0^{\circ}$	43
4.1	Schematic representation of a MPBVP	49
4.1	Single shooting differential correction procedure from a generic state	45
4.2	~ -	<b>~</b> 1
	$\vec{X}$ to a desired reference state $\vec{X}^*$ for a Hohmann transfer	51
5.1	GUI	
5.2	First manoeuvre	61
5.3	First propagation	63
5.4	Second manoeuvre	64

5.5	Second propagation	65
5.6	Third manoeuvre	66
5.7	Third propagation	68
5.8	Trajectory with open parachute	69
5.9	Last manoeuvre	70
5.10	Complete trajectory	71
5.11	Zoom in on the final landing phase	72

## Acronyms

BC

Boundary Condition

**FTDC** 

Fixed-Time Differential Correction

 $\mathbf{GUI}$ 

Graphical User Interface

IM

Indirect Method

LDW

Longitude-Dependent Waves

MAVEN

Mars Atmosphere and Volatile Evolution

MGCM

Mars General Circulation Model

MGS

Mars Global Surveyor

Mars-GRAM

Mars Global Reference Atmospheric Model

**MOLA** 

Mars Orbiter Laser Altimeter

#### **MPBVP**

Multi-Point Boundary Value Problem

#### MRO

Mars Reconnaissance Orbiter

### MTGCM

Mars Thermospheric General Circulation Model

### OCP

Optimal Control Problem

#### $\mathbf{OCT}$

Optimal Control Theory

### ODE

Ordinary Differential Equation

### ODY

Mars Odyssey

### PMP

Pontryagin's Maximum Principle

#### RS

Reference System

### SOI

Sphere of Influence

#### STM

State Transition Matrix

#### TES

Thermal Emission Spectrometer

### **TPBVP**

Two-Point Boundary Value Problem

### VTDC

Variable-Time Differential Correction

### ZEN

Zenit-East-North

## Chapter 1

## Introduction

### 1.1 Preface

One of the fundamental characteristics of human beings is the tendency to push beyond their visible boundaries, to explore the unknown, to reach unknown lands. Since prehistoric times, primitive man has moved from one territory to another to hunt, survive and exploit the natural resources present in the surrounding environment. At this stage, we cannot yet speak of "conquests" in the modern sense of the term, but this behaviour highlights an inner drive, guided by instinct and necessity.

Starting in the Metal Age, we begin to see true forms of conquest, with political and military significance. Civilisations such as the Sumerians and Egyptians began to expand their territories into unknown lands, giving rise to processes of not only territorial development, but also scientific and technological development. This expansion involved the need to overcome the limitations imposed by the human body, finding solutions to move more quickly or cope with hostile environments. In this sense, humans learned to exploit the natural elements to their advantage: sea currents, favourable winds, as well as knowledge of the most suitable times to travel, for example, avoiding the hottest hours in the desert.

This drive for expansion was not motivated solely by material needs, but also by a deep curiosity: the desire to know, to discover if there was anything beyond their known world. Although this attitude of intellectual inquiry emerged particularly in Greek culture, especially with Herodotus, considered the "father of history" [1] and the first traveller driven by a desire for exploration [2], it was already present in ancient civilisations, where exploration took the form of openness to the different and the new.

The conquests of antiquity did not take place with the support of modern tools such as detailed maps or satellite positioning systems. Instead, men relied on visual

memory, natural landmarks and previously left traces, developing a sophisticated sense of direction and a deep knowledge of the territory.

Just as in ancient times, human beings ventured beyond known boundaries to explore new lands, today we turn our gaze towards the universe. Space exploration is a continuation of the instinct that drove the peoples of the past to wonder about what exists beyond known territories: to understand the nature of other planets, to know if other forms of life exist or have existed, and to learn for the pure pleasure of doing so.

Unlike the explorations of antiquity, today we have detailed knowledge of the dangers to be faced, both during the journey and once we reach our destination. Modern space missions are based on careful planning, taking advantage of the most favourable launch windows and making use of simulations, data and cutting-edge technology. Human beings no longer move solely on instinct, but approach every step of exploration with scientific awareness and technical preparation.

In this context, Mars is now the main target for expansion. The desire to set foot on its surface is what drives me to write this thesis.

One of the most significant challenges facing humans in the exploration of Mars is that of entry, descent and landing on the red planet. The aim of this thesis is to propose a strategy for controlled landing that allows satellites and landers to reach the Martian surface safely and without damage.

To this end, the use of a hybrid propulsion system will be studied, characterised by an initial low-thrust braking phase and a high-thrust terminal phase. This solution optimises the management of the vehicle's overall mass, reducing the amount of propellant required and thus reserving more space for the payload, a crucial element for the success of the mission.

## 1.2 Optimization for Spacecraft Trajectories

The objective of this thesis is to minimise the consumption of propellant required to perform a transfer manoeuvre from a low Martian orbit to the planet's surface. Thanks to the contribution of Russian physicist Konstantin Eduardovich Tsiolkovsky, who formulated the Rocket Equation (1.1) in his work "Exploration of Cosmic Space by Means of Reaction Devices" [3], it was possible to express the relationship between the initial mass and final mass of the vehicle as a function of the ratio between the effective exhaust velocity, which measures how effectively the expelled propellant mass is used, and the velocity change required by the mission, i.e. the 'propulsion cost'.

$$\frac{m_0}{m_f} = e^{\frac{\Delta V}{c}} \tag{1.1}$$

Throughout this section, the concepts of effective exhaust velocity c and specific impulse  $I_{sp}$  will be used interchangeably, as they are directly proportional to each other. Specific impulse is defined as:

$$I_{sp} = \frac{c}{g_0} \tag{1.2}$$

where  $g_0$  represents the acceleration due to gravity at sea level on Earth. Specific impulse is expressed in seconds and represents a measure of engine efficiency: for the same propellant mass, a higher value allows the same thrust to be obtained for a longer time. Similarly, a higher exhaust velocity allows greater thrust to be generated in the same time interval. Chemical propulsion systems are characterised by low specific impulses, typically between 250 s and 350 s, reaching up to about 450 s in the case of high-efficiency liquid propellants, such as LOX/LH<sub>2</sub>. They are capable of generating large amounts of energy in a short time, but are intrinsically limited by the maximum chemical energy available in the reaction, as approximately expressed by the relationship (1.3).

$$c \approx \sqrt{2E_{ch}} \tag{1.3}$$

Where  $E_{ch}$  represents the specific chemical energy of the propulsion system [4]. A significant advantage of chemical propulsion systems lies in their scalability: the energy is contained within the propellant itself, making it possible to build engines of different sizes, capable of operating with highly variable flow rates and thrusts (from mN to MN).

To overcome the high propellant consumption associated with these systems, electric propulsion can be used, which is characterised by much higher specific impulses. However, the thrust generated is generally very low, and acceleration is continuous and prolonged (in the order of hours, days or weeks), typically requiring a higher  $\Delta V$  due to losses accumulated over time. Despite this, these systems offer a high level of precision and are a viable alternative for missions where time is not a limiting factor.

The numerical methods developed to solve these types of boundary value problems are direct methods and indirect methods.

Direct methods address the problem by transcribing it into subclasses subject to algebraic constraints; subsequently, all functions are discretised. The accuracy of the solution obtained depends on the density of the discretisation: the higher the density, the greater the accuracy, but the number of variables required will also increase, making the calculation computationally burdensome.

However, an advantage of these methods is that they do not require a complete

understanding of the problem or boundary conditions to obtain acceptable discrete solutions.

In contrast, indirect methods are faster, as they require fewer variables and return optimal solutions, provided they are initialised correctly. These methods are based on the introduction of additional variables and Lagrange multipliers, which lead to the formulation of an augmented problem. However, indirect methods are extremely sensitive to initial conditions, so they can suffer from poor convergence.

A comprehensive comparison of direct and indirect methods is provided in the work of Betts [5].

## 1.3 Overview of Chapters

Here a brief overview of the thesis contents is outlined.

Chapter 2 introduces the dynamic model of motion: the basics of celestial mechanics are reviewed, then the Reference Systems (RS) adopted are defined, namely the Mars-centred inertial system and the local system ZEN (Zenith–East–North), and the equations of motion are derived in spherical coordinates with projection of velocities and thrust. The chapter concludes with a review of the main perturbations, although only atmospheric resistance is adopted in the simulations.

Chapter 3 is dedicated to atmospheric density perturbation, which is the most relevant factor for the simulations in this work. The calculation of aerodynamic drag in the chosen RS is discussed, and the modelling of Martian atmospheric density using the Mars-GRAM [6] software is analysed, which allows the density to be estimated as a function of latitude, longitude and altitude.

Chapter 4 presents Optimal Control Theory (OCT) and illustrates how a dynamic problem can be reformulated as an Optimal Control Problem (OCP). After comparing direct and indirect methods, the focus shifts to the indirect approach and the formulation of the MPBVP. The necessary mathematical tools, such as added variables and optimality conditions, are described, and the multi-point optimal control problem is explored in depth, with the related differential correction techniques (single and multiple shooting) and the distinction between variable-time and fixed-time formulations. The chapter concludes with the application of these tools to the case study.

Chapter 5 illustrates and analyses the results obtained using the tool developed. It describes the evolution of the trajectory and mass variations, discussing the characteristics and effectiveness of the solutions identified in relation to the set

objectives and highlighting the contribution of the different propulsion phases.

Finally, Chapter 6 summarises the conclusions of the study. It highlights the main strengths, together with the limitations due to the simplifications of the model adopted, and proposes possible future developments to make the dynamic model increasingly realistic.

## Chapter 2

## Dynamic Model

This chapter presents the dynamic model adopted to describe the motion of a vehicle, starting from the fundamental laws of celestial mechanics and arriving at the operational formulation of the equations of motion used in simulations. The aim is to provide a logical path that, starting from physical principles, leads to a system of equations consistent with the reference choices and simplifying assumptions specific to the discussion.

The chapter begins with Newton's law of universal gravitation, which establishes the nature of the attractive field and allows us to write down the forces acting between point masses. On this basis, the N-body problem is introduced, highlighting how the nonlinear coupling of the equations generally makes an exact analytical solution impossible for N > 2, thus motivating the use of reduced models or numerical methods. The case is then specialised to the two body problem, in which an analytical solution is obtained in terms of conic sections. In this context, the constants of motion, mechanical energy and angular momentum, and the vis-viva relation, which are useful for classifying trajectories, are introduced. To link the analytical description of the orbit to the numerical formulation of the model, the chapter precisely defines the RS used. In particular: (i) the equatorial Mars-centred inertial system, with respect to which the three fundamental vectors of orbital mechanics are defined (specific angular momentum  $\vec{h}$ , node vector  $\vec{n}$  and eccentricity  $\vec{e}$ ) and therefore the six classical orbital elements  $(a, e, i, \Omega, \omega, \nu)$ ; (ii) the perifocal system, natural for expressing position and velocity on the Keplerian orbit; (iii) the Mars-centred polar system with velocities projected in the local triplet ZEN, adopted as the operational reference for time integration. We then move on to the construction of the equations of motion in the chosen reference. Finally, the chapter outlines the non-Keplerian effects. Although the simulations in this thesis adopt a perturbative model focused solely on Martian atmospheric resistance, an overview is provided of the main physical contributions that can

influence orbital evolution: non-sphericity of the gravitational field, third-body interactions and solar radiation pressure.

### 2.1 Newton's Gravitational Law

Isaac Newton, through his principles of dynamics, laid the foundations of classical mechanics. However, perhaps his most significant legacy from an astrodynamic point of view is the *law of universal gravitation* [7], which explains the gravitational interaction between bodies and provides a description of the orbital motion of celestial bodies.

The law of universal gravitation states that:

Two point masses A and B, with masses  $m_A$  and  $m_B$  respectively, exert an attractive force  $\vec{F}_g$  on each other, directed along the line connecting the two points. The magnitude of this force is directly proportional to the product of the masses and inversely proportional to the square of their distance.

This law can be expressed mathematically as:

$$\vec{F}_g = -G \frac{m_A m_B}{r^2} \,\hat{r} \tag{2.1}$$

where:

- $\vec{F}_q$  is the gravitational force
- G is the universal gravitational constant, whose value is  $G = 6.67 \times 10^{-11} \frac{\text{m}^3}{\text{kg s}^2}$
- $\vec{r}$  is the vector connecting the two masses, and  $r = |\vec{r}|$  is their distance
- $\hat{r} = \frac{\vec{r}}{r}$  is the unit vector along the connecting line.

Figure 2.1 shows the interaction between a satellite and the Earth, illustrating the application of the law of universal gravitation.

## 2.2 N-Body Problem

#### 2.2.1 Absolute motion

To study the absolute motion of celestial bodies, reference is made to the equations of dynamics in an inertial RS, i.e. a system that is stationary with respect to the

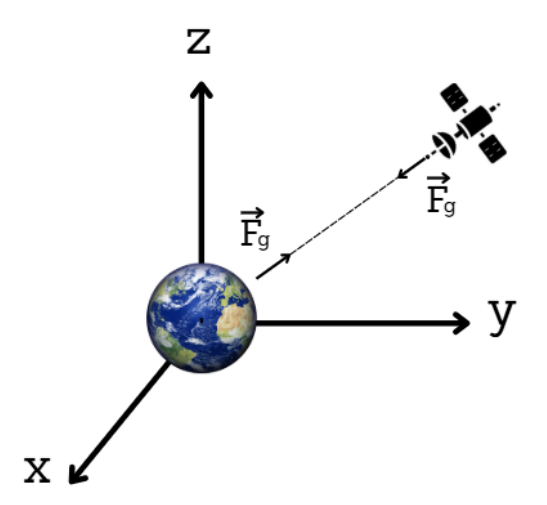


Figure 2.1: Gravitational interaction between two point masses

so-called fixed stars or moves in a uniform rectilinear motion. Although "fixed stars" do not exist in an absolute sense, they are so far away that they appear practically motionless to the observer, making them a useful reference for analysing motion.

To simplify the study of the gravitational system consisting of multiple bodies (known as the N-body problem), certain assumptions are made:

- Point masses: it is assumed that the entire mass of each body is concentrated at its centre of mass.
- Constant masses: it is assumed that masses do not change over time.
- Gravitational forces only: the presence of forces other than gravitational forces is disregarded.

The equation of motion for the generic body i of the system is therefore:

$$m_i \ddot{\vec{R}}_i = \vec{F}_1 + \vec{F}_2 + \dots + \vec{F}_j + \vec{F}_N$$
 (2.2)

where the force exerted by body i on body i is given by:

$$\vec{F}_{ij} = -G \frac{m_i m_j}{|\vec{R}_i - \vec{R}_j|^2} \cdot \frac{\vec{R}_i - \vec{R}_j}{|\vec{R}_i - \vec{R}_j|}$$
(2.3)

This equation describes a non linear, coupled dynamic system, whose complexity increases rapidly with the number of bodies involved. Already for N > 2, the

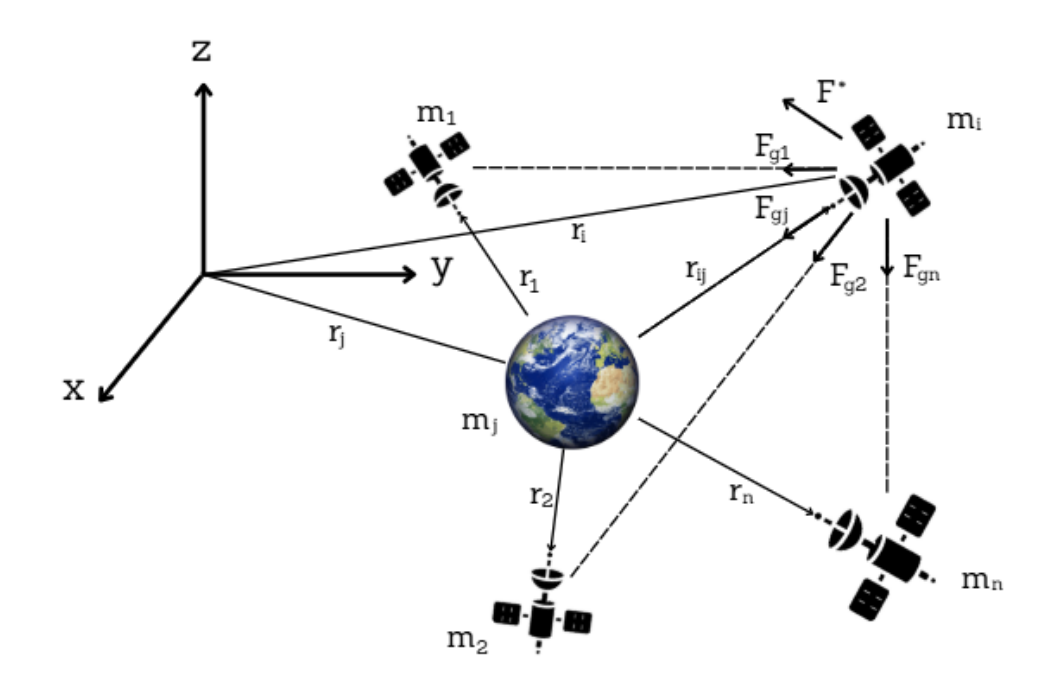


Figure 2.2: Gravitational interactions in an N-body system

behaviour of the system can no longer be treated analytically in an exact manner. A simple integration of the equation of motion is not possible, since the acceleration  $\vec{R}_i$  of the *i*-th body depends not only on its position  $\vec{R}_i$ , but also on those of all other bodies  $\vec{R}_j$  with  $j \neq i$ . More precisely, the gravitational force acts as a function of the relative distance between the bodies and varies dynamically over time as the bodies move. The force, therefore, is not constant, and the system evolves continuously with a strong dependence on the initial conditions. Furthermore, since this is a system with coupled second-order equations, solving the entire problem requires not only writing a system of N vector equations, but also addressing them jointly, since each is influenced by all the others.

From a computational point of view, the vectors can be split into three Cartesian scalar components (x, y, z), transforming each vector equation into three scalar equations. However, this leads to an increase in the total number of equations: from N vector equations to 3N scalar equations, which remain coupled and of the second order.

In summary, there is no general analytical solution for the N body problem. The only viable way to obtain an approximate solution is to use numerical integration methods, which allow the system to evolve over time with a precision determined

by the choice of method and time step used.

#### 2.2.2 Relative motion

The main interest in studying the motion of celestial bodies often does not concern their movement with respect to an absolute inertial RS, but rather their relative motion with respect to a central body, such as the Sun in the case of the solar system. From this perspective, the number of equations to be considered is reduced from N to N-1, as one of the equations is absorbed into the relative reference. A particularly important situation is the so-called restricted N-body problem, which arises when one of the bodies (of mass  $m_j$ ) is much less massive than the others, i.e.  $m_j \ll m_1, m_2, \ldots, m_{N-1}$ . In this case, it is assumed that the body of negligible mass does not influence the motion of the other bodies, but still undergoes their gravitational attraction.

A further simplification occurs in the two body problem, which represents a special but fundamental case for many applications, such as the Earth–Sun system or a spacecraft–Earth system. This model is characterised by the presence of a main body, significantly more massive than the other, and has an exact analytical solution.

Although simplified, this type of modelling forms the theoretical basis for classical orbital dynamics and is the starting point for the analysis of space trajectories, interplanetary missions and orbital manoeuvres.

## 2.3 Two Body Problem

In the two body problem model, further simplifying assumptions are made, partly derived from the N-body problem, such as the assumption of point masses and spherical symmetries. Furthermore, the system considered consists of two masses: a primary mass (of mass M) and a secondary mass (of mass m), where the latter is negligible compared to the former m << M. Finally, it is assumed that the interaction between the two bodies occurs only through gravitational force, neglecting the effects of perturbative forces and those due to other bodies present in the system.

The system is described in an inertial RS, as illustrated in the Figure 2.3 The force by which the two bodies attract each other is identical in magnitude and direction, but opposite in verse, and is, according to equation (2.1), directly proportional to their masses and inversely proportional to the square of their distance, where  $\vec{r} = \vec{\rho} - \vec{R}$ , as shown in the following equation:

$$|F_m| = |F_M| = G\frac{mM}{r^2} \tag{2.4}$$

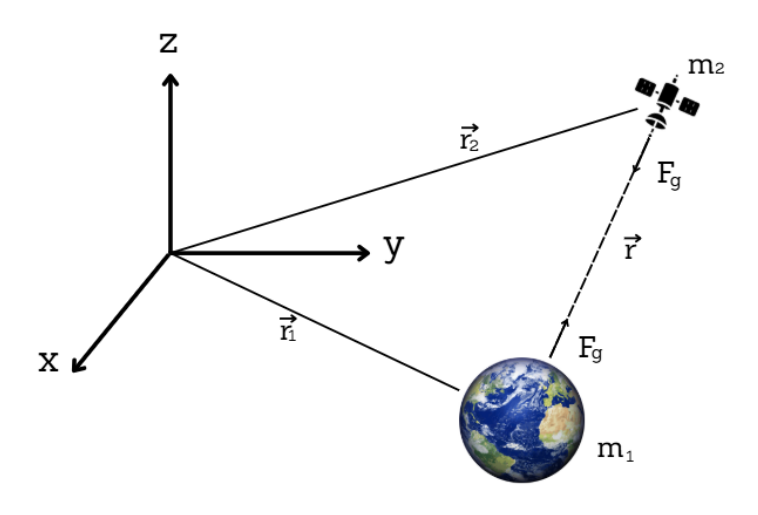


Figure 2.3: Gravitational interactions in a two body system

#### 2.3.1 Equation of motion

The equation of motion can be obtained by writing the equation of motion for each body relative to the inertial frame RS. In this way, the equilibrium between the product of mass and acceleration relative to the inertial frame RS and the gravitational force acting on each body is established. Therefore, for each of the masses, the following equations are obtained:

$$m\ddot{\vec{\rho}} = -G\frac{mM}{r^2}\frac{\vec{r}}{r} \tag{2.5a}$$

$$m\ddot{\vec{\rho}} = -G\frac{mM}{r^2}\frac{\vec{r}}{r}$$

$$M\ddot{\vec{R}} = G\frac{mM}{r^2}\frac{\vec{r}}{r}$$
(2.5a)

Subtracting equations (2.5a) and (2.5b), and simplifying appropriately, we arrive at the overall motion equation (2.6). In this expression, we consider that the secondary mass m is negligible compared to the primary mass M, and we observe that the difference between the accelerations of the two bodies in the inertial frame RS is equivalent to the acceleration of the secondary body relative to the main body. Therefore, we obtain:

$$\ddot{\vec{\rho}} - \ddot{\vec{R}} = -G \frac{M + m \vec{r}}{r^2} \frac{\vec{r}}{r}$$

$$\ddot{\vec{r}} \approx -\frac{GM \vec{r}}{r^2} \frac{\vec{r}}{r}$$
(2.6)

Where  $GM = \mu$  represents the gravitational parameter, which depends on the mass of the primary body, and its unit of measurement is  $[\mu] = [\text{km}^3/\text{s}^2]$ . In this way, we arrive at the equation of motion of the secondary body relative to the primary body in the two body problem. Solving equation (2.7), we obtain the position of the body of mass m relative to the body of mass M.

$$\ddot{\vec{r}} + \frac{\mu}{r^2} \frac{\vec{r}}{r} = 0 \tag{2.7}$$

By integrating the equation of motion obtained previously, we can derive the equation of the trajectory, which describes a conic section. However, before proceeding with the calculation of the trajectory, it is necessary to determine two constants of motion, which provide crucial information about the nature of the orbit: mechanical energy and angular momentum.

In the context of the two body problem, mechanical energy is conserved, except for perturbing forces, and is the sum of kinetic energy and gravitational energy. Mechanical energy is expressed by the following formula:

$$\mathscr{E} = \frac{V^2}{2} - \frac{\mu}{r} \tag{2.8}$$

Equation (2.8) is known as vis-viva, relating orbital velocity V, radial distance r and gravitational parameter  $\mu$ . The sign of the mechanical energy allows us to classify the type of orbit: if  $\mathcal{E} < 0$ , the orbit is an ellipse or a circle; if  $\mathcal{E} = 0$ , the orbit is a parabola; if  $\mathcal{E} > 0$ , the orbit is a hyperbola. Mechanical energy can also be expressed as a function of the semi-major axis a of the conic:

$$\mathscr{E} = -\frac{\mu}{2a} \tag{2.9}$$

In this formulation, it is clear that the shape of the trajectory is identified by the sign and value of a: for a > 0, the orbit is closed; for  $a \to \infty$ , the trajectory is open and a parabola is obtained; while for a < 0, the trajectory is open and a hyperbola is obtained.

Another parameter that is conserved during the motion of a body under gravitational influence, barring perturbations, is angular momentum, defined as the vector product of the radius and velocity of the body:

$$\vec{h} = \vec{r} \times \vec{V} \tag{2.10}$$

Equation (2.10) implies that, at every point along the trajectory, the product of the radius and the velocity is constant, which means that the angular momentum is conserved during the motion of the body.

To derive the equation of the trajectory, it is necessary to perform the vector product between the angular momentum and each member of the equation (2.7). In this way, we obtain the equation of the trajectory (2.12):

$$\vec{h} \wedge \ddot{\vec{r}} = \vec{h} \wedge \left[ -\frac{\mu}{r^2} \frac{\vec{r}}{r} \right] \tag{2.11}$$

From which, after appropriate manipulations, the equation of the trajectory in polar form is obtained:

$$r = \frac{h^2/\mu}{1 + B/\mu \cdot \cos\nu} \tag{2.12}$$

In this expression, r represents the distance between the two bodies, h is the specific angular momentum,  $\mu$  is the gravitational parameter, and  $\nu$  is the true anomaly. The constant B depends on the initial conditions of the system and determines the shape of the orbit. Equation (2.12) assumes a minimum value if the function in the denominator is at its maximum, i.e. when  $\nu = 0$ .

### 2.3.2 Polar equation of a conic section

A conic section in the plane can be defined as the set of points such that the ratio between the distance of each point from a focus and its distance from the directrix is constant. This constant is called the eccentricity of the conic section.

Equation (2.12) can be rewritten in the canonical form of conic sections in polar coordinates:

$$r = \frac{p}{1 + e\cos(\nu)} \tag{2.13}$$

where  $p = h^2/\mu$  is the semi-major axis, which represents the distance between the focus and the point on the conic section identified by the intersection of the curve with the line perpendicular to the major axis passing through the focus, while  $e = B/\mu$  is the eccentricity of the conic section, which determines its geometric shape. In particular, as e varies, different types of trajectories can be distinguished: for e = 0, the curve is a circle; for 0 < e < 1, it is an ellipse; if e = 1, it is a parabola; and finally, for e > 1, it is a hyperbola.

In summary, the classification of orbital trajectories can be expressed in terms of

specific mechanical energy  $\mathcal{E}$ , semi-major axis a and eccentricity e, as shown in Table 2.1.

Mechanical Energy	Semi-major axis	Eccentricity	Conic
$\mathscr{E} < 0$	a > 0	e = 0	Circumference
$\mathcal{E} < 0$	a > 0	0 < e < 1	Ellipse
$\mathscr{E} = 0$	$a \to \infty$	e = 1	Parabola
$\mathcal{E} > 0$	a < 0	e > 1	Hyperbole

**Table 2.1:** Classification of conic sections based on  $\mathcal{E}$ , a, e

Starting from the classification of orbits based on specific mechanical energy and orbital parameters, it is possible to introduce some characteristic velocities, which represent limit or reference conditions for the motion of a body around the centre of attraction.

In particular, to maintain a circular orbit, a satellite must have the so-called circular velocity, always tangent to the trajectory and therefore perpendicular to the radius vector. As in a circular trajectory the distance from the centre of attraction remains constant, we have a = r. Substituting this relationship into the equation of vis-viva (2.8) and highlighting the orbital velocity V, we obtain:

$$v_c = \sqrt{\frac{\mu}{r}} \tag{2.14}$$

This relationship shows that circular velocity decreases as the orbital radius increases. Another particularly important characteristic velocity is escape velocity, defined as the minimum velocity required for a body to permanently escape the gravitational field of the central planet. It is obtained by equating the equation of vis-viva calculated at the point of interest with the same equation evaluated at the limit  $r \to \infty$ :

$$\frac{v_e^2}{2} - \frac{\mu}{r} = \frac{v_\infty^2}{2} - \frac{\mu}{r_\infty},\tag{2.15}$$

where  $v_{\infty}$  represents the residual velocity at infinite distance. In the limiting case  $v_{\infty} = 0$ , we obtain:

$$v_e = \sqrt{\frac{2\mu}{r}} = \sqrt{2}v_c. \tag{2.16}$$

In this scenario, the orbital mechanical energy is zero, a condition equivalent to  $a \to \infty$ , and the resulting trajectory is a parabola.

The concept of escape velocity is closely related to that of Sphere of Influence (SOI), which represents the volume of space within which the gravitational attraction of

the planet can be considered predominant over that of the main body (in the case of Earth, the Sun). The radius of the sphere of influence can be estimated using the following equation:

$$r_{SOI} = r_{12} \left(\frac{m_2}{m_1}\right)^{2/5},\tag{2.17}$$

where  $r_{12}$  is the average distance between the planet and the central body,  $m_2$  is the mass of the secondary body (Earth) and  $m_1$  is the mass of the central body (Sun).

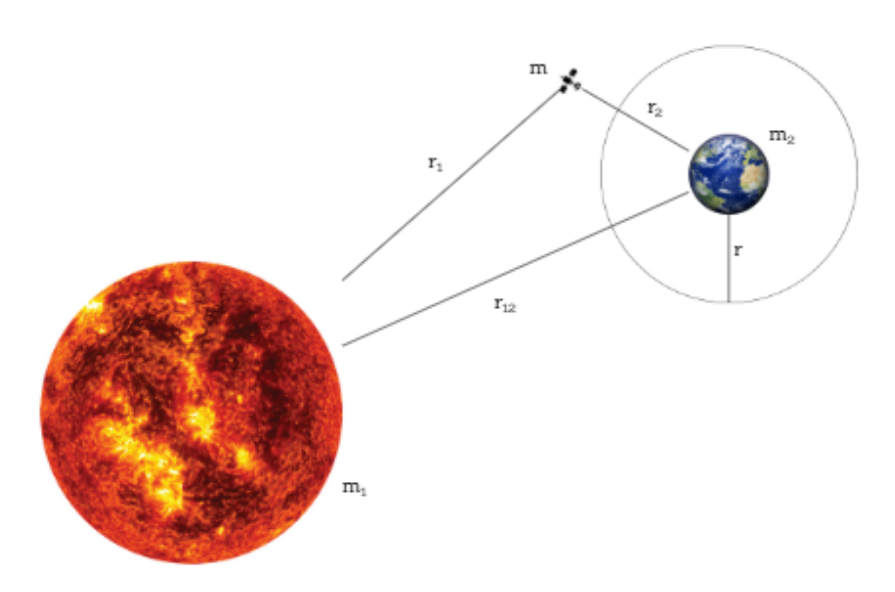


Figure 2.4: Assessment of the Sphere of Influence

For Earth, the value of SOI is  $r_{SOI} = 6.9 \times 10^5 \ km$ .

At last, we introduce the third characteristic velocity, known as hyperbolic excess velocity, which represents the residual velocity possessed by a body once it has left the sphere of influence of the planet. Unlike the parabolic case, where the final velocity at infinity is zero, here it is positive and is denoted by  $v_{\infty}$ .

$$v_{\infty} = \sqrt{-\frac{\mu}{a}} \tag{2.18}$$

For the root argument to be positive, a < 0 must hold, a condition that corresponds to a hyperbolic trajectory.

In the specific case of Earth, the characteristic velocities assume well-defined values, traditionally referred to as cosmic velocities. These values are summarised in Table 2.2.

Cosmic velocity	Value [km/s]
First cosmic velocity	7.91
Second cosmic velocity	11.19
Third cosmic velocity	16.65

Table 2.2: Cosmic velocities of the Earth

The first cosmic velocity corresponds to the minimum velocity required to describe a circular orbit around the Earth at zero altitude.

The second cosmic velocity is the velocity that allows a spacecraft to permanently leave the Earth's gravitational field, travelling along a parabolic or hyperbolic trajectory.

The third cosmic velocity represents the velocity that a spacecraft on the Earth's surface would need to have at launch in order to leave the sphere of influence of the Sun, i.e. to leave the Solar System.

## 2.4 Reference System

An RS is defined by an origin, a fundamental plane and an orthonormal triad associated with that plane. Choosing a suitable RS can greatly simplify the analysis and resolution of a specific problem. In this thesis, a RS in Mars-centred system polar coordinates was adopted to describe the position of the satellite, where r is the radius,  $\varphi$  is the latitude, and  $\vartheta$  is the longitude, while the velocity is projected into the local ZEN system. This topocentric, rotating and therefore non-inertial RS, identified by the triplet  $\{\hat{u}, \hat{v}, \hat{w}\}$ , allows the components of the probe's velocity along the radial, tangential and normal directions to be described in a natural way. The radial direction is defined by the vector connecting the centre of the planet with the instantaneous position of the probe, while the tangential and normal directions are orthogonal to it and are comparable, respectively, to the directions identified by a parallel and a meridian on the celestial sphere.

Before showing how the equations of motion are expressed in the RS adopted in this thesis, it is worth recalling the different systems used to describe orbital dynamics. Starting from the equation of motion derived in Section 2.3.1, it is possible to determine the orbital parameters that characterise the trajectory. Subsequently, these parameters are translated into coordinates for the perifocal system  $(\hat{p}, \hat{q}, \hat{w})$  and finally transformed into the RS chosen in this discussion, i.e. that defined by

polar coordinates for position and by the local system ZEN for velocity, passing through the equatorial Mars-centred system.

### 2.4.1 Orbital parameters

Before deriving the six classical orbital parameters, it is necessary to introduce three fundamental vectors  $(\vec{h}, \vec{n}, \vec{e})$ , expressed in their components with respect to the Mars-centred equatorial inertial frame RS (Figure 2.5). This system originates at the centre of Mars, with the Martian equator as its fundamental plane, and is defined by the orthonormal triplet  $(\hat{I}, \hat{J}, \hat{K})$ . The axis  $\hat{I}$  is directed towards the vernal equinox,  $\hat{K}$  is perpendicular to the equatorial plane and oriented along the Martian north pole, while  $\hat{J}$  completes the triad according to the right-hand rule.

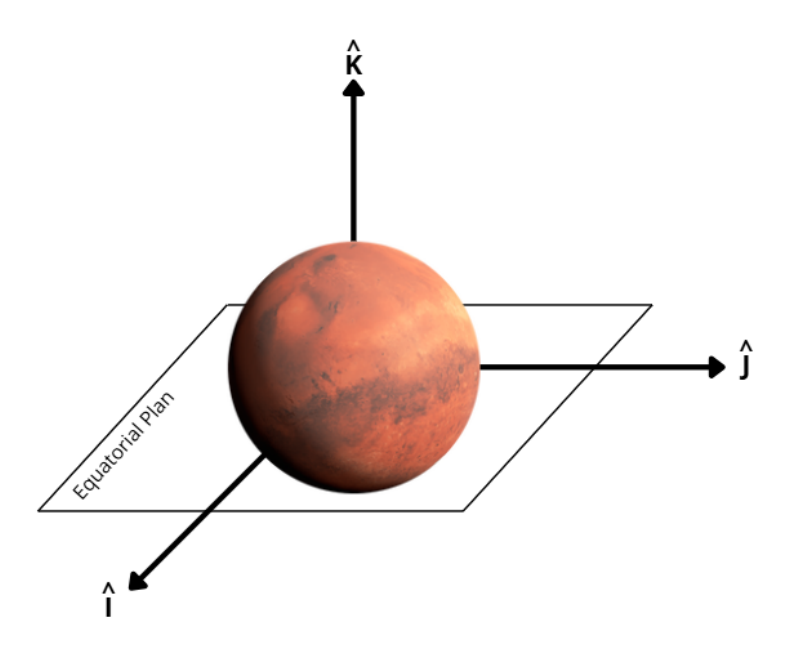


Figure 2.5: Mars RS  $(\hat{I}, \hat{J}, \hat{K})$ .

The first vector to be introduced is the specific angular momentum:

$$\vec{h} = \vec{r} \times \vec{v} = \begin{vmatrix} \hat{I} & \hat{J} & \hat{K} \\ r_I & r_J & r_K \\ v_I & v_J & v_K \end{vmatrix} = h_I \hat{I} + h_J \hat{J} + h_K \hat{K},$$
 (2.19)

which is perpendicular to the orbital plane and defines its orientation in space. The second vector is the node vector:

$$\vec{n} = \hat{K} \times \vec{h} = \begin{vmatrix} \hat{I} & \hat{J} & \hat{K} \\ 1 & 0 & 0 \\ h_I & h_J & h_K \end{vmatrix} = -h_J \hat{I} + h_I \hat{J},$$
 (2.20)

obtained as the vector product between the polar axis  $\hat{K}$  and the specific angular momentum. It lies on the equatorial plane and points along the line of nodes in the direction of the ascending node. Lastly, the eccentricity vector is defined:

$$\vec{e} = \frac{\vec{B}}{\mu} = \frac{\vec{v} \times \vec{h}}{\mu} - \frac{\vec{r}}{r},\tag{2.21}$$

pointing from the centre of the planet towards the periastron of the orbit. Its modulus coincides with the value of the orbital eccentricity, providing a direct measure of the shape of the trajectory.

Figure 2.6 (taken from [8]) shows the geometric representation of the three vectors  $\vec{h}$ ,  $\vec{n}$  and  $\vec{e}$  within the inertial RS, highlighting the relationships with the equatorial plane and with the orbital parameters that will be introduced later.

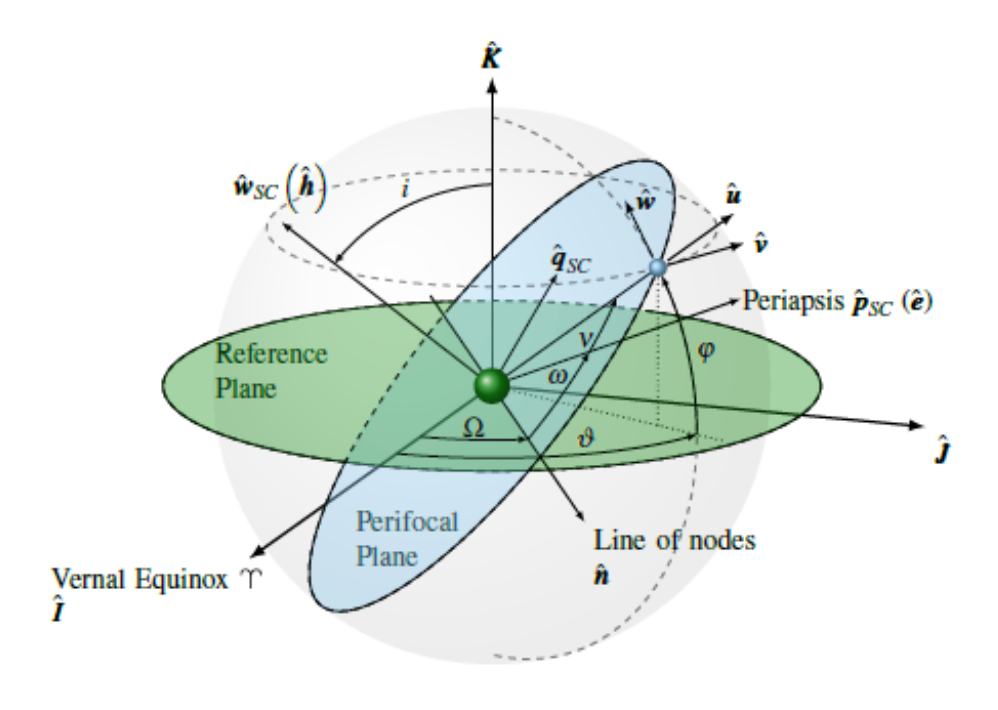


Figure 2.6: Orbital parameters

Once that three fundamental vectors  $(\vec{h}, \vec{n}, \vec{e})$  are defined, the orbital element can be easily calculated, as can be seen in the Table 2.3 (taken by [9]):

Parameter	Definition
Semi-major axis $a$	$\mathscr{E} = -\frac{\mu}{2a}$
Eccentricity $e$	$e = \ \vec{e}\ $
Inclination $i$	$\cos i = \frac{\vec{h} \cdot \hat{K}}{h} = \frac{h_K}{h}$
RAAN $\Omega$	$\cos \Omega = \frac{h}{\vec{I} \cdot \vec{n}} = \frac{n_I}{n}$
Argument of perigee $\omega$	$\cos \omega = \frac{\vec{n} \cdot \vec{e}}{ne}$
True anomaly $\nu$	$\cos \nu = \frac{\vec{e} \cdot \vec{r}}{er}$

**Table 2.3:** Definition of the six classical orbital elements

The element a determines the size of the orbit, while the eccentricity e defines its shape. The inclination i identifies the inclination of the orbital plane with respect to the equatorial reference plane and is always between  $0^{\circ}$  and  $180^{\circ}$ . The longitude of the ascending node  $\Omega$  represents the angle between the reference axis  $\hat{I}$  and the direction of the ascending node; in particular, if  $n_J > 0$ , then  $0^{\circ} < \Omega < 180^{\circ}$ , while if  $n_J < 0$ , then  $180^{\circ} < \Omega < 360^{\circ}$ . The argument of perihelion  $\omega$  is defined as the angle between the ascending node and the perihelion: if  $e_K > 0$ , then  $0^{\circ} < \omega < 180^{\circ}$ , while if  $e_K < 0$ , then  $180^{\circ} < \omega < 360^{\circ}$ . Finally, the true anomaly  $\nu$  is the angle between the perigee and the instantaneous position of the satellite along the orbit at a given moment in time; if  $\vec{r} \cdot \vec{v} > 0$ , then  $0^{\circ} < \nu < 180^{\circ}$ , while if  $\vec{r} \cdot \vec{v} < 0$ , then  $180^{\circ} < \nu < 360^{\circ}$ .

## 2.4.2 Equation of motion in spherical coordinates

Given the six orbital parameters  $a, e, i, \Omega, \omega, \nu$ , it is possible to determine the position vector and velocity vector in the perifocal RS. They are expressed respectively as

$$\vec{r}_{pqw} = \begin{bmatrix} r \cos \nu \\ r \sin \nu \\ 0 \end{bmatrix}, \qquad \vec{v}_{pqw} = \begin{bmatrix} -\sqrt{\frac{\mu}{p}} \sin \nu \\ \sqrt{\frac{\mu}{p}} (e + \cos \nu) \\ 0 \end{bmatrix}, \qquad (2.22)$$

where the vector radius r is calculated using the conic equation (2.13), while the semi-major axis is defined as  $p = a(1-e^2)$  [9]. The perifocal RS describes the motion of the satellite in a natural way. Its origin coincides with the centre of the central body, located at the focus of the orbit, and is defined by the orthonormal triplet  $\{\hat{p}_{SC}, \hat{q}_{SC}, \hat{w}_{SC}\}$ , shown in Figure 2.7 (taken from [8]). The versor  $\hat{p}_{SC}$  is oriented along the direction of the eccentricity vector  $\vec{e}$ , while  $\hat{w}_{SC}$  is perpendicular to the orbital plane and coincides with the direction of the specific angular momentum vector  $\vec{h}$  (Figure 2.6). Finally,  $\hat{q}_{SC}$  completes the triplet according to the right-hand rule.

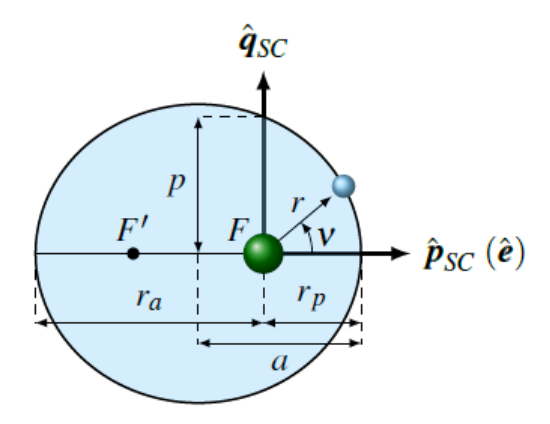


Figure 2.7: Perifocal RS

Using the rotation matrix shown in Appendix A, it is possible to transform the coordinates from the perifocal system to the Mars-centred equatorial inertial system. Applying the matrix  $L_{pqw\to IJK}$ , we obtain the relationships between the position and velocity vectors expressed in the two RS:

$$\vec{r}_{IJK} = L_{pqw \to IJK} \ \vec{r}_{pqw}, \qquad \vec{v}_{IJK} = L_{pqw \to IJK} \ \vec{v}_{pqw}, \tag{2.23}$$

where  $\vec{r}_{IJK} = (x, y, z)$  and  $\vec{v}_{IJK} = (\dot{x}, \dot{y}, \dot{z})$  represent the Cartesian components of the position vector and velocity vector, respectively. Once these components are known, it is possible to determine the associated spherical coordinates, i.e. the radius r, the declination  $\varphi$  and the right ascension  $\vartheta$ , using the following expressions:

$$r = \sqrt{x^2 + y^2 + z^2}, \quad \vartheta = \text{atan2}(y, x), \quad \varphi = \text{atan2}(z, \sqrt{x^2 + y^2})$$
 (2.24)

As illustrated in Figure 2.8, the position vector can therefore be rewritten in spherical form:

$$\vec{r} = r \begin{bmatrix} \cos\varphi \cos\theta \\ \cos\varphi \sin\theta \\ \sin\varphi \end{bmatrix}. \tag{2.25}$$

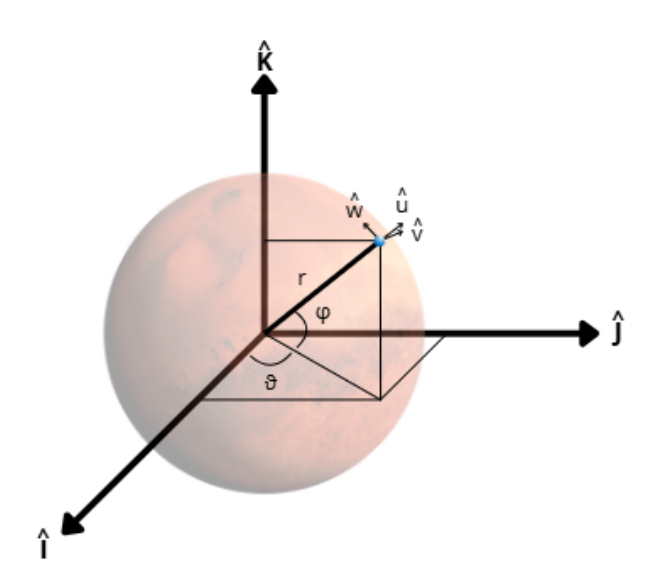


**Figure 2.8:** Representation of the position vector in spherical coordinates within the Mars-centred equatorial inertial RS

Deriving equation of position vector in spherical coordinates gives the Cartesian velocity:

$$\vec{v} = \dot{\vec{r}} = \begin{bmatrix} \dot{r}\cos\varphi\cos\vartheta - r\,\dot{\vartheta}\sin\vartheta\cos\varphi - r\,\dot{\varphi}\cos\vartheta\sin\varphi \\ \dot{r}\cos\varphi\sin\vartheta + r\,\dot{\vartheta}\cos\vartheta\cos\varphi - r\,\dot{\varphi}\sin\vartheta\sin\varphi \\ \dot{r}\sin\varphi + r\,\dot{\varphi}\cos\varphi \end{bmatrix}. \tag{2.26}$$

By projecting  $\vec{v}$  onto the local triplet  $\{\hat{e}_r, \hat{e}_{\vartheta}, \hat{e}_{\varphi}\}$  (defined in Appendix B) via scalar product, we obtain the components

$$v_r = \vec{v} \cdot \hat{e}_r = \dot{r} = u \tag{2.27a}$$

$$v_{\vartheta} = \vec{v} \cdot \hat{e}_{\vartheta} = r \, \dot{\vartheta} \cos \varphi = v$$
 (2.27b)

$$v_{\varphi} = \vec{v} \cdot \hat{e}_{\varphi} = r \ \dot{\varphi} = w \tag{2.27c}$$

from which the three kinematic relationships are derived:

$$\frac{dr}{dt} = u \tag{2.28a}$$

$$\frac{d\vartheta}{dt} = \frac{v}{r\cos\varphi} \tag{2.28b}$$

$$\frac{d\varphi}{dt} = \frac{w}{r} \tag{2.28c}$$

Deriving  $\vec{v}$  gives the acceleration in spherical coordinates:

$$\vec{a} = \frac{d}{dt}(v_r\hat{e}_r + v_\vartheta\hat{e}_\vartheta + v_\varphi\hat{e}_\varphi) = \dot{v}_r\,\hat{e}_r + v_r\,\dot{\hat{e}}_r + \dot{v}_\vartheta\,\hat{e}_\vartheta + v_\vartheta\,\dot{\hat{e}}_\vartheta + \dot{v}_\varphi\,\hat{e}_\varphi + v_\varphi\,\dot{\hat{e}}_\varphi, \quad (2.29)$$

which, by explicitly developing the time derivatives of the local unit vectors (defined in Appendix B) and appropriately reordering the terms obtained, leads to the following compact expression of the acceleration in the three directions of the spherical basis:

$$\vec{a} = (\dot{v}_r - v_\vartheta \,\dot{\vartheta}\cos\varphi - v_\varphi \,\dot{\varphi})\,\hat{e}_r + (\dot{v}_\vartheta + v_r \,\dot{\vartheta}\cos\varphi - v_\varphi \,\sin\varphi \,\dot{\vartheta})\,\hat{e}_\vartheta + (\dot{v}_\varphi + v_r \,\dot{\varphi} + v_\vartheta \,\sin\varphi \,\dot{\vartheta})\,\hat{e}_\varphi.$$
(2.30)

Expressed in terms of the components (u, v, w) defined above, the kinematic equations for accelerations become

$$\frac{du}{dt} = \frac{v^2}{r} + \frac{w^2}{r} \tag{2.31a}$$

$$\frac{dv}{dt} = -\frac{uv}{r} + \frac{wv}{r}\tan\varphi \tag{2.31b}$$

$$\frac{dw}{dt} = -\frac{uw}{r} - \frac{v^2}{r} \tan \varphi \tag{2.31c}$$

which represent purely geometric terms (no force applied).

In the central gravitational model, Mars' acceleration is radial and values  $-\mu/r^2$  along  $-\hat{e}_r$ . To this are added the perturbative accelerations  $(a_p)_r, (a_p)_\vartheta, (a_p)_\varphi$  and, if present, the components of thrust  $(T_u, T_v, T_w)$  projected onto the spherical base. The dynamic system in Mars-centred polar coordinates for position and in ZEN for velocity is therefore:

$$\begin{cases}
\frac{dr}{dt} = u \\
\frac{d\theta}{dt} = \frac{v}{r\cos\varphi} \\
\frac{d\varphi}{dt} = \frac{w}{r} \\
\begin{cases}
\frac{du}{dt} = -\frac{\mu}{r^2} + \frac{v^2}{r} + \frac{w^2}{r} + \frac{T_u}{m} + (a_p)_u \\
\frac{dv}{dt} = -\frac{uv}{r} + \frac{vw}{r}\tan\varphi + \frac{T_v}{m} + (a_p)_v \\
\frac{dw}{dt} = -\frac{uw}{r} - \frac{v^2}{r}\tan\varphi + \frac{Tw}{m} + (a_p)_w \\
\frac{dm}{dt} = -\frac{T}{c}
\end{cases}$$
(2.32)

The components of the thrust T projected onto the local reference system ZEN can be expressed as:

$$T_u = T \sin \alpha_T, \tag{2.33a}$$

$$T_v = T \cos \alpha_T \cos \beta_T, \tag{2.33b}$$

$$T_w = T \cos \alpha_T \sin \beta_T. \tag{2.33c}$$

where  $\alpha_T$  represents the thrust angle in the local plane, while  $\beta_T$  defines the thrust deviation out of the plane.

## 2.5 Perturbing Forces

So far, the only reference has been to ideal orbits, i.e. Keplerian orbits, described in the context of simplifying assumptions that characterise the treatment of the two body problem. In reality, however, these assumptions do not hold: none of the six classical orbital parameters is constant over time.

Actual orbits can be described as Keplerian orbits subject to perturbations due to the presence of non-Keplerian forces. In the two body model, all orbital parameters are invariant over time, with the exception of the true anomaly, which varies naturally with orbital motion, except in the case of transfer manoeuvres. In reality, however, this variation is superimposed by additional effects: on the one hand, a secular drift is observed, characterised by a monotonic, generally linear variation of the orbital parameters; on the other hand, periodic oscillations may occur, which can be divided into short-period oscillations, due to phenomena that repeat at each revolution, and long-period oscillations, linked to the interaction and variation of

the different parameters.

An example of this behaviour is shown in Figure 2.9, which shows the evolution of orbital inclination. In a purely Keplerian model, the inclination would remain constant, while in the presence of perturbations it exhibits a secular drift associated with both long- and short-term oscillations.

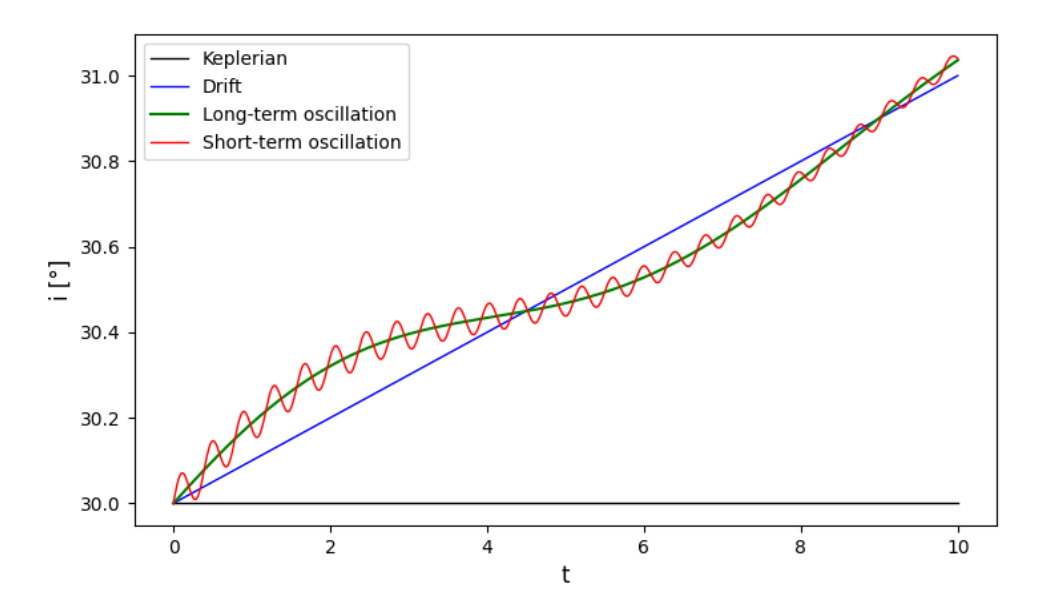


**Figure 2.9:** Evolution of the orbital inclination over time: comparison between the Keplerian case and the perturbative effects

Therefore, we can no longer refer to a perfect Keplerian orbit, but instead introduce the concept of an osculating orbit, i.e. an instantaneous Keplerian orbit that represents the state of the body at a given moment.

The equation of motion, including perturbative effects, can be expressed as:

$$\ddot{\vec{r}} = -\frac{\mu^2}{r^2} \frac{\vec{r}}{r} + \vec{a}_p \tag{2.34}$$

where  $\vec{a}_p$  represents the acceleration due to perturbing forces. In the dynamic model adopted in this thesis, the only perturbing effect considered is the acceleration due to the presence of the Martian atmosphere. For the sake of completeness, however, other possible sources of perturbation will also be mentioned, such as the non-sphericity of the planet, third-body interactions due to both the gravitational attraction of the Sun and that of the natural satellites Phobos and Deimos, and, finally, solar radiation.

The total perturbing acceleration can be expressed as the sum of the main contributions:

$$\vec{a}_p = \vec{a}_{drag} + \vec{a}_{J2} + \vec{a}_{3b} \tag{2.35}$$

### 2.5.1 Atmospheric drag

Atmospheric drag is a disruptive force that acts on the satellite's momentum, causing a change in its velocity. In the case of Mars, due to the low atmospheric density, the effect of drag is only significant at relatively low altitudes and becomes negligible above approximately 120–150 km. As reported in [10], the acceleration due to atmospheric drag can be expressed as:

$$\vec{a}_{drag} = -\frac{1}{2} \frac{C_D A}{m} \rho v_{rel}^2 \frac{\vec{v_{rel}}}{v_{rel}}$$
 (2.36)

The effect of atmospheric drag depends on several parameters that are difficult to estimate accurately. These include the aerodynamic drag coefficient,  $C_D$ , which varies depending on the satellite configuration (typically  $C_D \approx 2.0-2.2$ ), atmospheric density,  $\rho$ , which is highly dependent on altitude and environmental conditions and whose calculation is described in detail in Chapter 3, and the exposed cross-sectional area, A, which is related to the aircraft's attitude.

The relative velocity to be considered is that with respect to the atmosphere and not simply the orbital velocity, since the atmosphere rotates with Mars and is subject to phenomena such as winds. The velocity vector relative to the rotating atmosphere is:

$$\vec{v}_{rel} = \frac{d\vec{r}}{dt} - \vec{\omega}_{\oplus} \times \vec{r} = \begin{bmatrix} \frac{dx}{dt} + \vec{\omega}_{\sigma} y \\ \frac{dy}{dt} - \vec{\omega}_{\sigma} x \\ \frac{dz}{dt} \end{bmatrix}$$
(2.37)

where  $\vec{\omega}_{\sigma}$  represents the angular velocity of Mars. The relative velocity can be further refined by including the effect of atmospheric winds. A more general formulation, proposed by Pedro Ramon Escobal [11], is as follows:

$$\vec{v}_{rel} = \begin{bmatrix} \frac{dx}{dt} + \omega_{\oplus}y + v_w\{-\cos(\alpha)\sin(\delta)\cos(\beta_w) - \sin(\alpha)\sin(\beta_w)\} \\ \frac{dy}{dt} - \omega_{\oplus}x + v_w\{-\sin(\alpha)\sin(\delta)\cos(\beta_w) + \cos(\alpha)\sin(\beta_w)\} \\ \frac{dz}{dt} + v_w\{\cos(\delta)\cos(\beta_w)\} \end{bmatrix}$$
(2.38)

where  $v_w$  represents the wind speed,  $\beta_w$  its azimuth, while  $\alpha$  and  $\delta$  are respectively the right ascension and declination of the satellite. In this study, the component due to atmospheric winds has been neglected, thus adopting the expression of (2.37) for the calculation of the relative velocity.

Since the position of the satellite is expressed in Mars-centred polar coordinates, where r is the radius,  $\varphi$  is the latitude and  $\vartheta$  is the longitude, while the velocity is projected into the local ZEN system, it is necessary to transform the position and velocity appropriately into the same RS used in (2.37), i.e. the Cartesian one  $(\hat{I}, \hat{J}, \hat{K})$ .

$$\begin{cases} x = r \cos\varphi \cos\theta \\ y = r \cos\varphi \sin\theta \\ z = r \sin\varphi \end{cases}$$
 (2.39)

The velocity is projected from ZEN to Cartesian coordinates by:

$$\vec{v}_{IJK} = L_{ZEN \to IJK} \ \vec{v}_{ZEN} \tag{2.40}$$

where  $v_{ZEN} = [u \ v \ w]^T$  and  $L_{ZEN\to IJK}$  is the rotation matrix defined in Appendix A. After calculating the components of atmospheric drag acceleration in the Cartesian inertial system, these must be converted back to the polar system with velocities expressed in ZEN, in order to be consistent with the dynamic model adopted. The inverse transformation is obtained by transposing the matrix  $L_{ZEN\to IJK}$ :

$$\vec{a}_{ZEN} = L_{ZEN \to IJK}^T \, \vec{a}_{IJK} \tag{2.41}$$

### 2.5.2 Mars asphericity

Another significant source of perturbation is the non-sphericity of Mars' gravitational field. In fact, like Earth, the Red Planet cannot be considered a perfectly spherical body, but rather an areoid characterised by flattening at the poles and irregularities due to the non-uniform distribution of internal masses. The perturbed gravitational potential can be expressed in the general form:

$$E_{gp} = -\frac{\mu_{\mathcal{S}}}{r} \left\{ 1 - \sum_{n=2}^{\infty} J_n \left( \frac{R_{\mathcal{S}}}{r} \right)^n P_n(\sin \varphi) + \sum_{n=2}^{\infty} \sum_{m=2}^{\infty} \left( \frac{R_{\mathcal{S}}}{r} \right)^n J_{nm} P_n^m(\sin \varphi) \cos[m(\vartheta - \vartheta nm)] \right\}$$
(2.42)

where  $J_n$  are the coefficients of the zonal harmonics, which describe axial deviations from spherical symmetry,  $P_n$  are Legendre polynomials of order n related to latitude,

 $J_{nm}$  are tesseral harmonics, if  $n \neq m$ , or sectorial harmonics, if n = m, and  $P_n^m$  are associated Legendre polynomials of order n and degree m. Legendre polynomials are defined as:

$$P_n(x) = \frac{1}{2^n n!} \frac{d^n}{dx^n} (x^2 - 1)$$
 (2.43a)

$$P_n^m(x) = (-1)^m (1 - x^2)^{m/2} \frac{d^m}{dx^m} [P_n(x)]$$
 (2.43b)

Among the various terms, the one that produces the dominant effect is the oblateness coefficient  $J_2$ , which represents the flattening of the planet at the poles and the consequent deviation of the potential from the spherical case. The influence of  $J_2$  introduces secular and periodic variations in the orbital parameters, with particularly significant effects on the longitude of the ascending node  $\Omega$  and on the argument of periastron  $\omega$ .

### 2.5.3 Third-body perturbations

The perturbative effects induced by a third body, such as the Sun or the natural satellites Phobos and Deimos, become particularly relevant at high altitudes, when atmospheric resistance progressively loses importance. Figure 2.10 illustrates the geometric configuration: the satellite of mass m orbits around the main body M (Mars), while also being affected by the gravitational pull of a perturbing body  $m_p$ , in this case represented by Phobos.

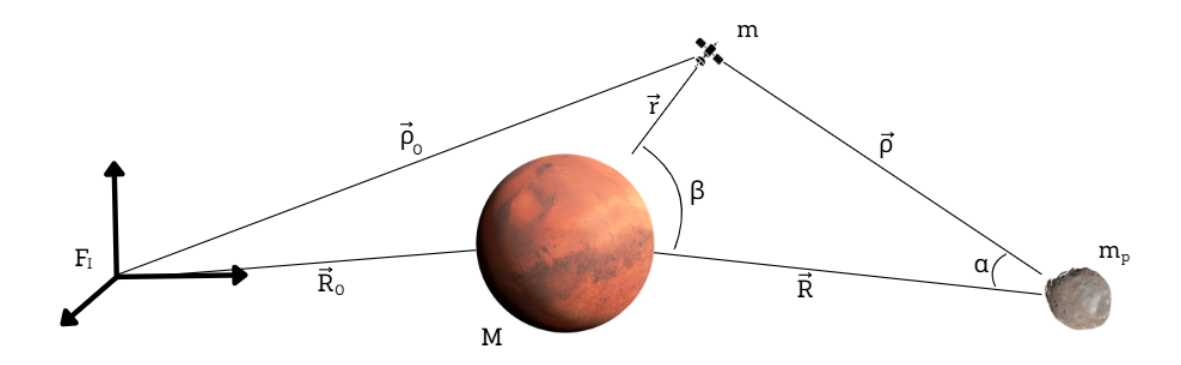


Figure 2.10: Third-body interaction scheme

The distance between M and m is defined by the vector  $\vec{r} = \vec{\rho} - \vec{R} = \vec{\rho}_0 - \vec{R}_0$ , while the geometric relationships between the three bodies are governed by:

$$r\cos\beta + \rho\cos\alpha = R \quad \rightarrow \quad \frac{\rho}{R}\cos\alpha = 1 - \frac{r}{R}\cos\beta$$
 (2.44)

where  $\alpha$  and  $\beta$  are the angles formed by the perturbing body and the satellite with respect to Mars.

Starting from the equation of motion for an *n*-body system, we can write the acceleration of the positions  $\ddot{\vec{\rho}}_0$  and  $\ddot{\vec{R}}_0$  with respect to the inertial frame RS:

$$\ddot{\vec{\rho}}_0 = -\frac{GM}{r^2} \frac{\vec{r}}{r} - \frac{Gm_p}{\rho^2} \frac{\vec{\rho}}{\rho}$$
 (2.45a)

$$\ddot{\vec{R}}_0 = -\frac{GM}{r^2} \frac{\vec{r}}{r} - \frac{Gm_p}{R^2} \frac{\vec{R}}{R}$$
 (2.45b)

Subtracting equation (2.45b) from (2.45a) gives the equation of motion for the satellite subject to the simultaneous attraction of Mars and the perturbing body:

$$\ddot{\vec{r}} = -\frac{\mu}{r^2} \frac{\vec{r}}{r} - \frac{\mu_p}{\rho^2} \frac{\vec{\rho}}{\rho} + \frac{\mu_p}{R^2} \frac{\vec{R}}{R}$$
 (2.46)

where the first term corresponds to the two body problem (Mars–satellite), while the remaining two describe the gravitational interaction of the third body. It is important to note that the perturbative acceleration does not derive directly from the attractive force of the perturbing body on the satellite, but rather from the difference in the forces exerted on the satellite and the central body, respectively. To quantify this perturbative acceleration, Carnot's theorem can be applied to the triangle formed by Mars, the satellite and the perturbing body:

$$a_p = \frac{\mu_p}{\rho^2} \sqrt{1 - 2\frac{\rho^2}{R^2} \cos\alpha + \frac{\rho^4}{R^4}}$$
 (2.47)

The discussion is divided into two cases. In the first case, if  $\rho \ll R$ , the satellite is very close to the perturbing body: the perturbative acceleration can then be approximated as  $a_p \simeq \mu_p/\rho^2$ , a condition that corresponds to the so-called classical three-body problem. In the second case,  $\rho \simeq R$ , or  $r/R \ll \varepsilon$ , the relation (2.44) becomes

$$\frac{\rho}{R}\cos\alpha = 1 - \varepsilon\cos\beta \tag{2.48}$$

Replacing in (2.47) and developing using Newton's series expansion, we obtain the expression for the perturbative acceleration of the third body

$$a_p = \mu_p \frac{r}{R^3} \sqrt{1 + 3\cos^2\beta} \tag{2.49}$$

The magnitude of the acceleration varies depending on the angle  $\beta$ : in the conjunction configuration ( $\beta = 0, \pi$ ) it assumes the maximum value  $a_p = \mu_p 2r/R^3$ , while in quadrature ( $\beta = \pi/2$ ), it is reduced to  $a_p = \mu_p r/R^3$ .

In general, the perturbative action of a third body is more significant the greater the distance of the satellite from the central body.

Table 2.4 shows a comparison between the gravitational and perturbative accelerations exerted by Mars, the Sun and the two natural satellites Phobos and Deimos, referring to a satellite located at an altitude of 140 km from the Martian surface. With regard to the accelerations due to perturbing bodies, the quadrature case was considered.

Gravitational acceleration $[km/s^2]$	Perturbative acceleration $[km/s^2]$
$a_{\text{C}} = \frac{\mu_{\text{C}}}{r^2} = 3.43 \times 10^{-2}$	_
$a_{\odot} = \frac{\mu_{\odot}}{\rho_{\odot}^2} = 5.89 \times 10^{-6}$	$a_{p\odot} = \frac{\mu_{\odot} r}{\rho_{\odot}^3} = 1.39 \times 10^{-10}$
$a_{Phobos} = \frac{\mu_{Phobos}}{\rho_{Phobos}^2} = 8.08 \times 10^{-8}$	$a_{p_{Phobos}} = \frac{\mu_{Phobos} r}{\rho_{Phobos}^3} = 3.05 \times 10^{-8}$
$a_{Deimos} = \frac{\mu_{Deimos}}{\rho_{Deimos}^2} = 1.78 \times 10^{-10}$	$a_{p_{Deimos}} = \frac{\mu_{Deimos} r}{\rho_{Deimos}^3} = 2.68 \times 10^{-11}$

**Table 2.4:** Comparison between gravitational and perturbative accelerations

The analysis of the values reveals an interesting aspect: although Phobos is much less massive than the Sun, its gravitational acceleration on the satellite is about two orders of magnitude lower. However, due to its proximity to Mars, Phobos' perturbing action is about two orders of magnitude greater than that of the Sun, demonstrating how distance plays a decisive role in the intensity of the perturbation.

#### 2.5.4 Solar radiation

The last effect considered is that of solar radiation, whose intensity, similar to the case of third-body perturbations, is less significant at low altitudes, where atmospheric effects predominate. It represents the pressure exerted by solar radiation on any exposed surface, producing a change in momentum due to the impact of photons. The acceleration due to solar radiation pressure is expressed by:

$$a_{SR} = p C_R \frac{S}{m} \tag{2.50}$$

where  $C_R$  is the reflectivity coefficient, which depends on the optical properties of the spacecraft's surface, S is the exposed area, and m is the mass of the satellite. The term p represents the solar pressure, which decreases with the square of the distance from the Sun. At a distance of 1 astronomical unit, equal to the average distance between the Earth and the Sun, its value is approximately  $p = 4.5 \times 10^{-6} \text{ N/m}^2$ . In the case of Mars, the greater distance from the Sun results in a reduction in the pressure value, which is approximately  $p_{\sigma} = 1.94 \times 10^{-6} \text{ N/m}^2$ .

# Chapter 3

# Atmospheric Density

Atmospheric drag played a fundamental role in the mission, as it allowed the main objective to be pursued: reaching the surface of Mars at a speed close to zero. In addition to modifying the satellite's trajectory, allowing for a reduction in the overall mission time, aerodynamic drag played a crucial role in gradually slowing down the vehicle, making the final controlled descent phase possible.

This chapter aims to provide a comprehensive overview of the atmospheric drag modelling adopted in the study. It begins with the presentation of the method used to represent the interaction between the satellite and the Martian atmosphere, including the spatial density interpolation procedure. This is followed by an analysis of the Mars-GRAM model, with a focus on its fundamental characteristics. It should be noted that this section is not intended as a user guide to Mars-GRAM, as this aspect is already thoroughly documented in the official User Guide [6], but rather as a summary of the main features relevant to the present work. Finally, the chapter concludes with the analysis of the case study, where the numerical and graphical results are presented and discussed.

## 3.1 Modelling of Martian Atmospheric Density

To model the Martian atmosphere, software developed by NASA Mars-GRAM was used, which provides the values of the main atmospheric parameters, including density, based on altitude, longitude and latitude.

This tool was used to generate an output file, as shown in Figure 3.1, containing the data needed to characterise the atmospheric profile. Subsequently, using a trilinear interpolation process implemented in Python, this information was used to introduce a contribution of aerodynamic drag into the satellite's dynamics.

To accurately estimate local density, the data space was represented as a threedimensional matrix, as shown in Figure 3.2, as if Mars were surrounded by a three-dimensional grid, whose axes are defined by:

- altitude, ranging from 0 200 km,
- latitude, ranging from  $-90^{\circ}$  to  $90^{\circ}$ ,
- longitude, ranging from  $0^{\circ}$  to  $360^{\circ}$ .

Time	HgtMOLA LatPO	LonW	Denkgm3	Temp	EWind	NWind
0.	101.00 -90.00	0.00	1.622E-08	105.9	4.5	0.6
0.	101.00 -90.00	10.00	1.622E-08	105.9	4.5	0.6
0.	101.00 -90.00	20.00	1.622E-08	105.9	4.5	0.6
0.	101.00 -90.00	30.00	1.622E-08	105.9	4.5	0.6
0.	101.00 -90.00	40.00	1.622E-08	105.9	4.5	0.6
0.	101.00 -90.00	50.00	1.622E-08	105.9	4.5	0.6
0.	101.00 -90.00	60.00	1.622E-08	105.9	4.5	0.6
0.	101.00 -90.00	70.00	1.622E-08	105.9	4.5	0.6
0.	101.00 -90.00	80.00	1.622E-08	105.9	4.5	0.6
0.	101.00 -90.00	90.00	1.622E-08	105.9	4.5	0.6
0.	101.00 -90.00	100.00	1.622E-08	105.9	4.5	0.6
0.	101.00 -90.00	110.00	1.622E-08	105.9	4.5	0.6
0.	101.00 -90.00	120.00	1.622E-08	105.9	4.5	0.6
0.	101.00 -90.00	130.00	1.622E-08	105.9	4.5	0.6
0.	101.00 -90.00	140.00	1.622E-08	105.9	4.5	0.6
0.	101.00 -90.00	150.00	1.622E-08	105.9	4.5	0.6
0.	101.00 -90.00	160.00	1.622E-08	105.9	4.5	0.6
0.	101.00 -90.00	170.00	1.622E-08	105.9	4.5	0.6
0.	101.00 -90.00	180.00	1.622E-08	105.9	4.5	0.6
0.	101.00 -90.00	190.00	1.622E-08	105.9	4.5	0.6
0.	101.00 -90.00	200.00	1.622E-08	105.9	4.5	0.6
0.	101.00 -90.00	210.00	1.622E-08	105.9	4.5	0.6
0.	101.00 -90.00	220.00	1.622E-08	105.9	4.5	0.6
0.	101.00 -90.00	230.00	1.622E-08	105.9	4.5	0.6
0.	101.00 -90.00	240.00	1.622E-08	105.9	4.5	0.6

Figure 3.1: Example of an Output file generated by Mars-GRAM

Each node of the grid contains the density value calculated by Mars-GRAM; the density corresponding to the satellite position, determined by the state vector, is obtained by trilinear interpolation within the three-dimensional matrix.

In particular, the point of interest is identified within a cube defined by eight known density nodes, corresponding to two altitude values, two latitude values and two longitude values.

The trilinear interpolation process consists of several steps: initially, four linear interpolations are performed along a first direction, thus reducing the problem from three-dimensional to two-dimensional; subsequently, two interpolations are performed along the second direction, which reduce the problem to one dimension; finally, a last linear interpolation is applied along the third direction, obtaining the final density value at the required point.

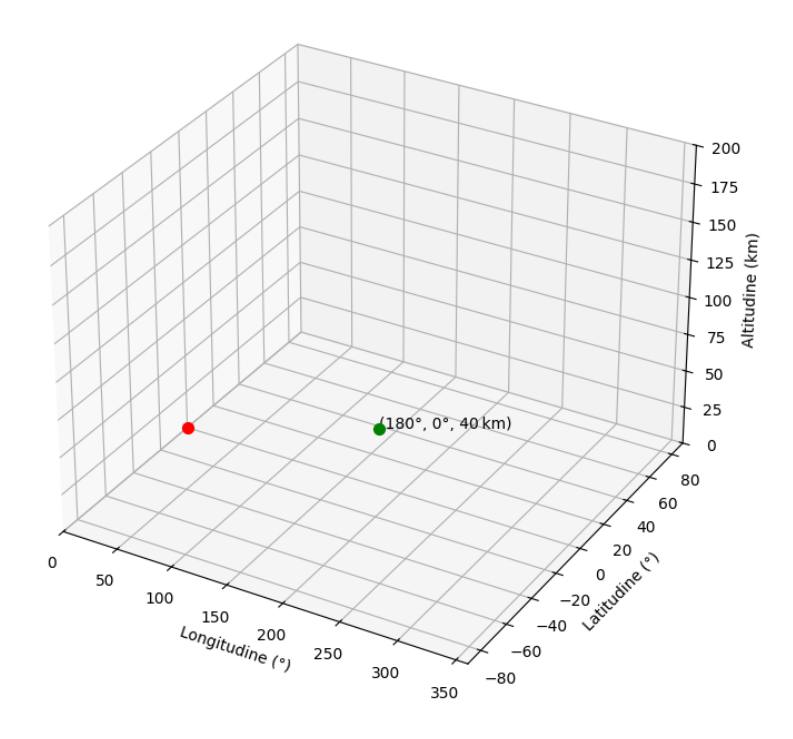


Figure 3.2: Cube for trilinear interpolation

# 3.2 Use of the Mars-GRAM Model for Atmospheric Analysis

Mars-GRAM is an atmospheric model developed by NASA, specifically by the NASA Marshall Space Flight Center. Some of the fundamental atmospheric models from which Mars-GRAM derives its data, such as the Mars General Circulation Model (MGCM) and the Mars Thermospheric General Circulation Model (MTGCM), were developed respectively by the NASA Ames Research Center and the University of Michigan.

Mars-GRAM was developed to support engineers and mission planners in the design of vehicles intended to enter and navigate within the Martian atmosphere. The model provides detailed values on atmospheric properties and related variations, including temperature, density, pressure and winds.

The software allows the user to set input parameters such as time, geographic position (altitude, longitude, and latitude), and atmospheric dust level, returning as output the values of atmospheric properties and composition. Mars-GRAM has been employed in numerous Martian aerobraking missions of probes such as Mars Global Surveyor (MGS), Mars Odyssey (ODY), Mars Reconnaissance Orbiter

(MRO), and the Mars Atmosphere and Volatile Evolution (MAVEN) mission. Mars-GRAM has undergone several updates over time. It was originally developed in Fortran in 1988 and has recently rewritten in C++ to improve computational efficiency and integration with other engineering tools. In particular, the new version includes integration with NASA's SPICE libraries, enabling more accurate computation of Martian ephemerides, as well as the introduction of a new CSV output format, better suited for data processing and visualization.

### 3.2.1 Mars-GRAM atmospheric data

Within the Mars-GRAM model, the atmospheric structure is defined by combining two models: the NASA Ames MGCM up to an altitude of 80 km, and the MTGCM for the upper layers. Both models use the topography derived from the MOLA (Mars Orbiter Laser Altimeter) altimeter of the MGS mission, referring to the constant equipotential surface known as the areoid.

Mars-GRAM allows the selection of different configurations of the average atmosphere through the MapYear input parameter, which identifies the Martian year of reference for the data.

- With MapYear = 0, the user can manually specify the optical depth of the dust and use interpolated MGCM data corresponding to three values of  $\tau$  ( $\tau = 0.3, 1.0, 3.0$ ).
- With MapYear = 1 or 2, the data are derived from MGCM simulations guided by actual measurements of optical depth made by the TES (Thermal Emission Spectrometer) instrument during Martian years 1 (1999-2001) and 2 (2001-2002).

Mars-GRAM also allows local atmospheric variations to be modelled using three disturbance scale parameters:

- DensityPerturbationScale, for density;
- EWWindPerturbationScale and NSWindPerturbationScale, for east—west and north—south winds;
- PerturbationWaveLengthScale, for the perturbation wavelength.

The planetary constants are taken from the NASA Space Science Data Coordinated Archive portal, specifically from the Planetary Fact Sheet for Mars section, as shown in Table 3.1.

Mars	Label	Units	Value
Gravitational Parameter	GM	$\mathrm{km}^3/\mathrm{s}^2$	42828.3736
Mean Equatorial Radius	$R_e$	$\mathrm{km}$	3396.2
Mean Polar Radius	$R_p$	$\mathrm{km}$	3376.2
J2 harmonic	$J_2$	$\mathrm{km}^{5}/\mathrm{s}^{2}$	0.00196045
Period		S	88642.44

**Table 3.1:** Mars gravity parameters

Topography Data The MOLA, aboard the MGS probe, provided high-resolution Martian topographic data, used in Mars-GRAM to define altitude relative to a geodetic reference known as the areoid, a gravitational equipotential surface. Starting with versions after 2001, Mars-GRAM adopts the MOLA topography and the related areoid with a grid resolution of half a degree in latitude and longitude by default. However, it is still possible to work with versions prior to 2001 with lower resolutions.

Atmospheric Input Models and Data The MGCM tables provide meteorological data as a function of altitude, longitude, latitude, and local time up to an altitude of 80 km, while the MTGCM tables extend this coverage from 80 to 170 km for MapYear = 0 and up to 240 km for MapYear = 1 or 2.

For altitudes above 170 km, Mars-GRAM uses a modified Stewart-type thermospheric model, which accounts for geographic variations and solar activity. This model becomes effective starting from a pressure level of 1.26 nbar, corresponding to an altitude known as the ZF height (typically around 125 km).

Between 80 km and the ZF height, Mars-GRAM relies on MTGCM data, which are interpolated or extrapolated as a function of the solar activity index F10.7, using reference datasets available for F10.7 = 70 and F10.7 = 130.

Finally, between the ZF height and 170 km, a gradual transition is carried out between the two models, ensuring continuity and consistency in atmospheric properties.

Interpolation Methods The atmospheric parameters in Mars-GRAM are obtained through multidimensional interpolation on MGCM/MTGCM gridded data, including logarithmic interpolation on optical depth and altitude interpolation that respects the barometric law and that of perfect gases. This approach ensures realistic and stable transitions between the different levels of the simulated atmosphere.

To realistically represent the strong thermal and dynamic discontinuities in the lower layer of the Martian atmosphere, Mars-GRAM uses a boundary layer model

based on a logarithmic profile corrected by the Richardson number. This approach allows for accurate simulation of the differences between ground and air temperatures as low as 5 metres above the ground, as well as the vertical reduction of wind components near the surface.

The model takes into account surface roughness  $(z_0)$ , assuming different values in the presence of ice, directly influencing the slope of the thermal profile and wind components in the sub-surface layer.

Longitude-Dependent Waves Mars-GRAM allows to include the effect of longitude-dependent waves (LDW), which are particularly relevant for orbital scenarios synchronous with the Sun. This model introduces periodic modulations of atmospheric density as a function of longitude and time, which can be customised via input files or external dynamic coefficients.

**Height Adjustment** One of the main challenges in Martian atmospheric modelling is ensuring physical and numerical continuity in the transition between models developed for different altitude ranges. Mars-GRAM addresses this issue by introducing altitude corrections that allow the interface to be adjusted at approximately 80 km altitude, where the transition from MGCM to MTGCM data occurs.

These corrections allow the height of atmospheric levels to be adjusted in order to maintain consistency between simulated and observed density profiles, for example during aerobraking missions. In particular, the latest versions of Mars-GRAM offer various options for calculating the height offset, from a simple constant correction (OffsetModel = 0) to more sophisticated models based on local and seasonal data (OffsetModel = 3 or 4).

Quantitative Dust Concentration Model A distinctive feature of Mars-GRAM is its ability to model dust storms on a global or regional scale in a parametric and highly controllable manner. Dust storms are one of the most critical aspects of the Martian atmosphere, as they can cause significant variations in atmospheric density, temperature, and the vertical distribution of dust itself. These variations directly affect aerodynamic operations (e.g., during atmospheric entry) and the performance of surface scientific instruments.

Mars-GRAM allows a storm to be defined by a series of physically meaning-ful parameters: intensity (StormIntensity), duration (StormDuration), location (StormLatitude, StormLongitude) and maximum radius (StormMaxRadius). When StormMaxRadius takes on high or zero values, the storm is treated as global, allowing extreme scenarios to be simulated. Intensity is expressed in terms of maximum optical depth, which is added to the background optical depth to determine the total optical depth  $\tau$ .

Mars-GRAM computes the vertical distribution of atmospheric dust from the

optical depth  $\tau$ , using formulas derived from the MGCM developed by Haberle et al [12]. The model assumes that the particles are spherical, with a typical diameter of 5  $\mu$ m and a density of 3,000 kg/m<sup>3</sup>. From these parameters and the vertical pressure distribution, Mars-GRAM derives:

- The areal density of dust on the ground (mass per unit area).
- The dust mixing ratio (mass per unit mass of air), calculated as a function of a parameter DustNu that controls the vertical profile.
- The particle number density (number of particles per  $m^3$ ), useful for evaluating optical and thermal phenomena.

Solar and Thermal Radiation Among the auxiliary programs available with Mars-GRAM, MarsRad.cpp makes it possible to compute the incoming and outgoing components of solar and thermal radiation, both at the surface and at the top of the atmosphere. It uses as input the CSV file generated by Mars-GRAM, which also includes dust concentrations, and is based on albedo values provided by the MOLA data.bin file.

Slope Wind Model The wind model in Mars-GRAM, implemented in the slopewind subroutine, is based on the work of Ye et al. [13] and uses MOLA topographic data with half-degree resolution to determine the slope of the terrain. The computed winds depend on altitude, slope, and local time, with a maximum vertical extent of 4.5 km during the day and 2.5 km during the night. They are added to the MGCM winds and also include a vertical component proportional to the slope and horizontal velocity. The activation and intensity of the model can be controlled via the BoundaryLayerWindsScale parameter.

## 3.3 Analysis of the Case Study Results

Before analysing some examples of variations in atmospheric density as a function of altitude, latitude and longitude, the procedure followed to generate the density data grid using the Mars-GRAM software is described.

### 3.3.1 Preparation and compilation of Mars-GRAM

To generate the output file shown in Figure 3.1, it was first necessary to prepare a trajectories file to be used as input to the auxiliary program BLDTRAJ.f90, specifying the reference elevations and the relative discretisation steps. In the case study considered, a maximum altitude of 200 km was adopted, with a step of 1 km;

longitude was varied over the interval  $0^{\circ}$ -360° with a step of 10°, while latitude was evaluated between  $-90^{\circ}$  and 90°. The resulting three-dimensional grid is shown in Figure 3.3.

```
C:\Users\achil\OneDrive\Desktop\Politecnico\Tesi\Mars-GRAM 2010\Release1.0_Nov10\Executables>BLDTRAJ.exe Enter trajectory file name
trajectory0_100
Enter z1,z2,dz (Real km)
0 100 1
Enter lat1,lat2,dlat (Real deg.)
-90 90 10
Enter lon1,lon2,dlon (Real deg.)
0 360 10
Enter time increment (Real sec)
0
Number height, lat, lon, total = 101 19 37 71003
Data written to file trajectory0_100
```

Figure 3.3: Output BLDTRAJ.f90

To simplify the calculation of atmospheric density, the altitude was divided into two separate ranges: the first up to 100 km and the second between 101 and 200 km. As for the time variable, a zero value was assigned, since in the case study, variations in parameters such as density and temperature during the Martian day were not considered. The values are therefore calculated with reference to the initial instant.

The next step is to have Mars-GRAM process the generated trajectory file, preparing an input file that includes, in addition to the trajectory, additional information necessary for the calculation. These include: the reference date and time, set to 6 May 2025, the level of solar activity, set close to the maximum for consistency with the chosen day (F10.7 = 130); and finally the parameters relating to atmospheric dust, assumed to be moderate, with values Dusttau = 0.5, Dustmin = 0.3 and Dustmax = 1.0, as shown in the Figure 3.4.

Finally, once the input file had been correctly created, it was possible to proceed with the compilation of Mars-GRAM, as shown in Figure 3.5.

# 3.3.2 Trend of atmospheric density as a function of spatial coordinates

To obtain a clearer picture of the distribution of Martian atmospheric density, an analysis was carried out on the density trend as a function of altitude, longitude and latitude. The data generated by the Mars-GRAM model were reprocessed using Python to obtain the profile trends, with the aim of highlighting any differences that could affect the dynamics of the satellite during descent.

```
$INPUT M10
 LSTFL
             'LIST.txt'
 OUTFL
             'OUTPUT.txt'
              trajectory0_100.txt
  TRAJFL
 profile
             'null'
 WaveFile
             'null'
              C:\Users\achil\OneDrive\Desktop\Politecnico\Tesi\Mars-GRAM 2010\Release1.0_Nov10\binFiles\
 GCMDIR
             C:\Users\achil\OneDrive\Desktop\Politecnico\Tesi\Mars-GRAM 2010\Release1.0_Nov10\binFiles\
 IERT
 IUTC
 MDAY
 MYEAR
 NPOS
 IHR
 IMIN
 SEC
 F107
 Dusttau
 Dustmin
```

Figure 3.4: Input file Mars-GRAM

```
C:\Users\achil\OneDrive\Desktop\Politecnico\Tesi\Mars-GRAM 2010\Release1.0_Nov10\Executables>marsgram_M10.exe
    Enter file name for NAMELIST input
inp6may25_0_100.txt

Mars-GRAM 2010 (Version 1.0) - Nov 2010
LIST file= LIST.txt

OUTPUT file= OUTPUT.txt

Data directory= C:\Users\achil\OneDrive\Desktop\Politecnico\Tesi\Mars-GRAM 2010\Release1.0_Nov10\binFiles\
GCM directory= C:\Users\achil\OneDrive\Desktop\Politecnico\Tesi\Mars-GRAM 2010\Release1.0_Nov10\binFiles\
Input data from Mapping Year = 0

Trajectory file= traj0_100.txt

Reading MOLA 1/2 degree areoid and topography
Reading 1 degree albedo data
Reading Mars GCM surface data files
Reading Mars GCM 0-80 km data files
Reading Mars TGCM 80-170 km data files
Reading Mars TGCM 80-170 km data files
Reading TES Yr1 & Yr2 MGCM 5-5 to 80 km data files
Reading TES Yr1 & Yr2 MGCM 5-5 to 80 km data files
Reading TES Yr1 & Yr2 MGCM 5-5 to 80 km data files
Fenished Setup_M10 - Starting computations

STOP Normal Termination
```

Figure 3.5: Mars-GRAM running

The graph in Figure 3.6 analyses the variation in density with latitude for different longitudes, keeping the altitude constant at 10 km.

The curves show a peak density between 30° South and the equator, followed by a gradual decrease towards northern latitudes. The density is not symmetrical with respect to the equator: this could be due to the asymmetrical distribution of atmospheric dust or local topographical variations.

Similarly, the plots in Figures 3.7 analyse the behaviour of density as a function of altitude, this time keeping the latitude constant (equal to 0°) and varying the longitude. The complete graph again shows an exponential decrease with altitude, common to all profiles. However, slight differences can be observed in the lower part of the atmosphere, which become evident in the zoom shown in the second figure (3.7b).

Between 0 and 10 km altitude, some longitudes (e.g.,  $300^{\circ}$  and  $330^{\circ}$ ) have slightly higher densities than others, such as  $90^{\circ}$  or  $270^{\circ}$ . These differences may be due

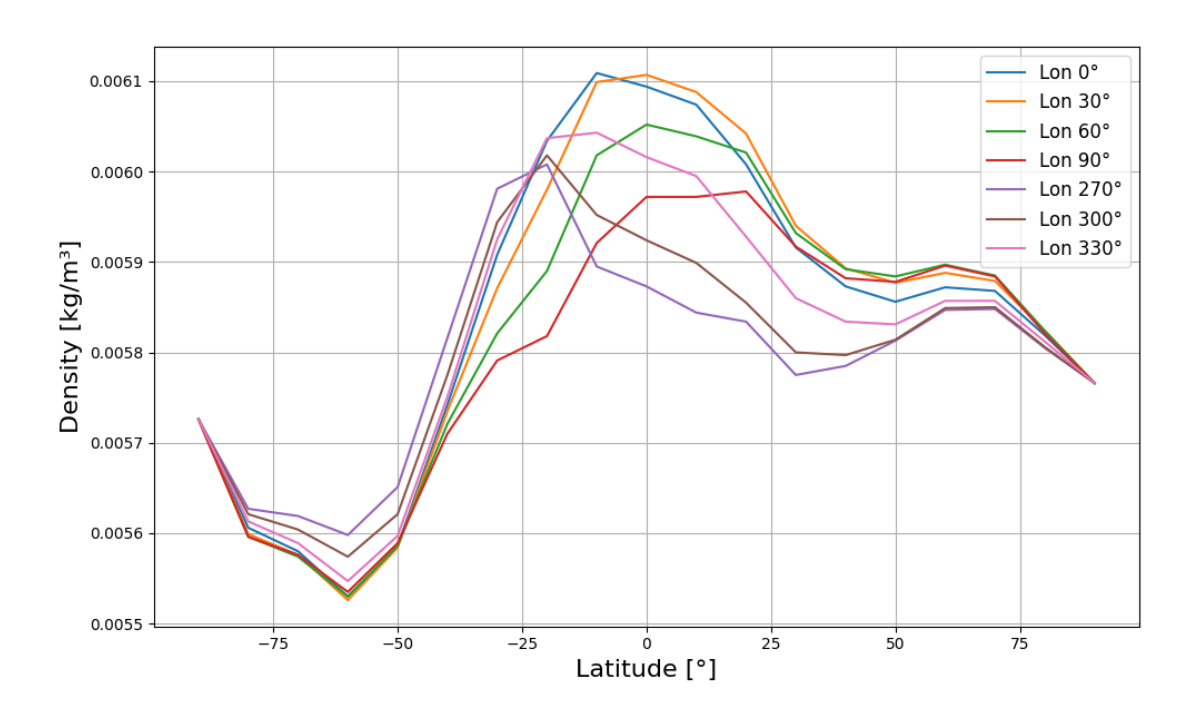


Figure 3.6: Atmospheric density profiles on Mars at altitude = 10 km

to the presence of plateaus or depressions, variations in surface albedo, or effects related to local atmospheric circulation. Although the differences are small, it is important to note that in the simulation of aerodynamic drag, even minimal variations can have a significant impact on orbital dynamics at low altitudes.

The plot in Figure 3.8a shows the vertical profile of Martian atmospheric density as altitude varies, keeping longitude constant (equal to  $0^{\circ}$ ) and varying latitude. As expected, the density decreases exponentially with altitude. The differences between the curves are minimal, but they are slightly more evident in the first few kilometres above the surface.

Figure 3.8b, which is a zoom of the previous graph, highlights these local variations in the lower atmospheric layer (below 10 km). In this region, the curves for the lower latitudes (southern hemisphere) tend to show a slightly higher density than those for the northern hemisphere. This effect can be attributed to the fact that, on the date considered (6 May 2025), Mars is near its perihelion. In this orbital configuration, corresponding to the southern summer, the southern hemisphere receives more solar energy. This leads to a more pronounced warming of the atmosphere, which tends to expand, generating higher density values at the same altitude than in the opposite hemisphere [14].

The plot in Figure 3.9 shows the trend in Martian atmospheric density as a

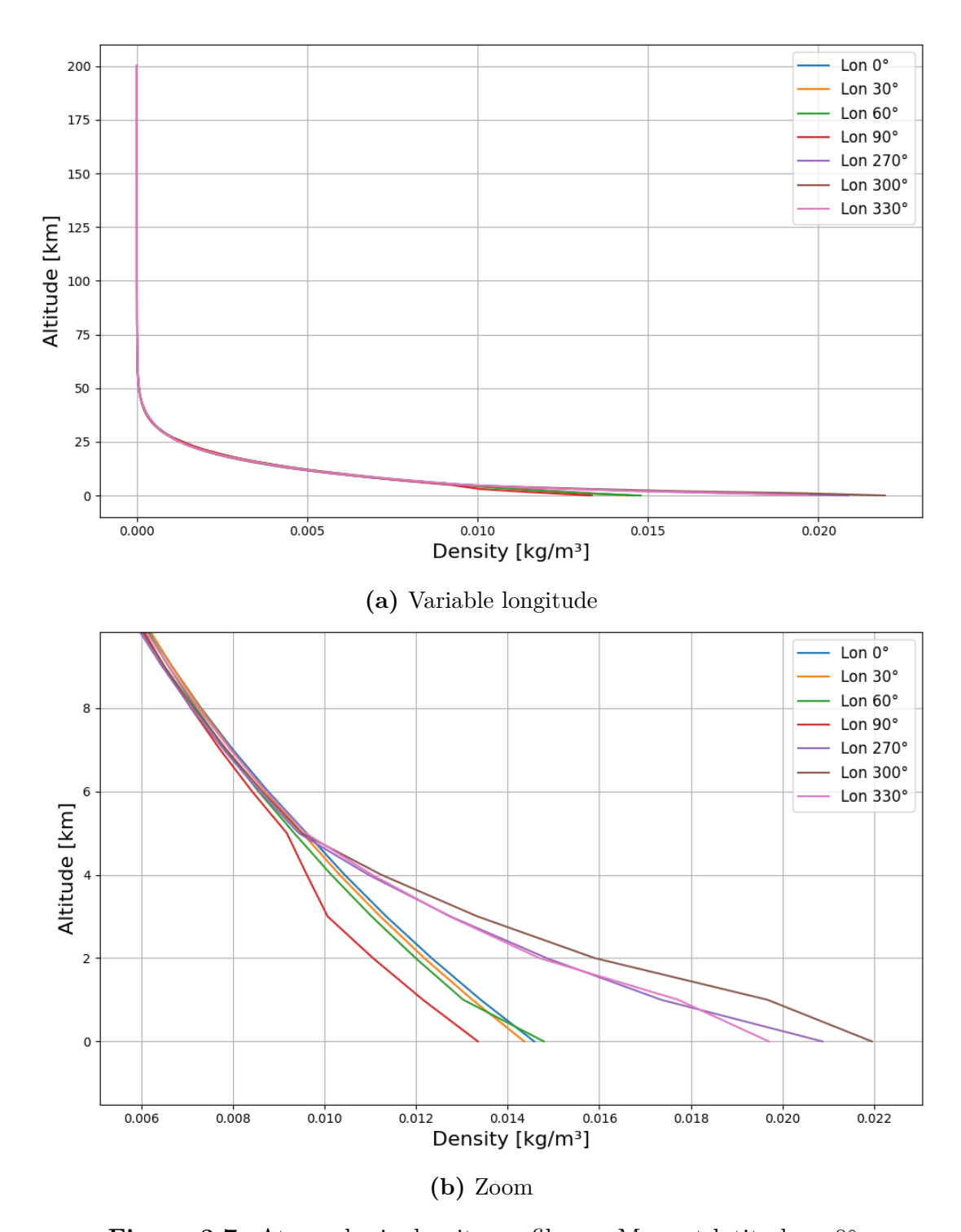


Figure 3.7: Atmospheric density profiles on Mars at latitude =  $0^{\circ}$ 

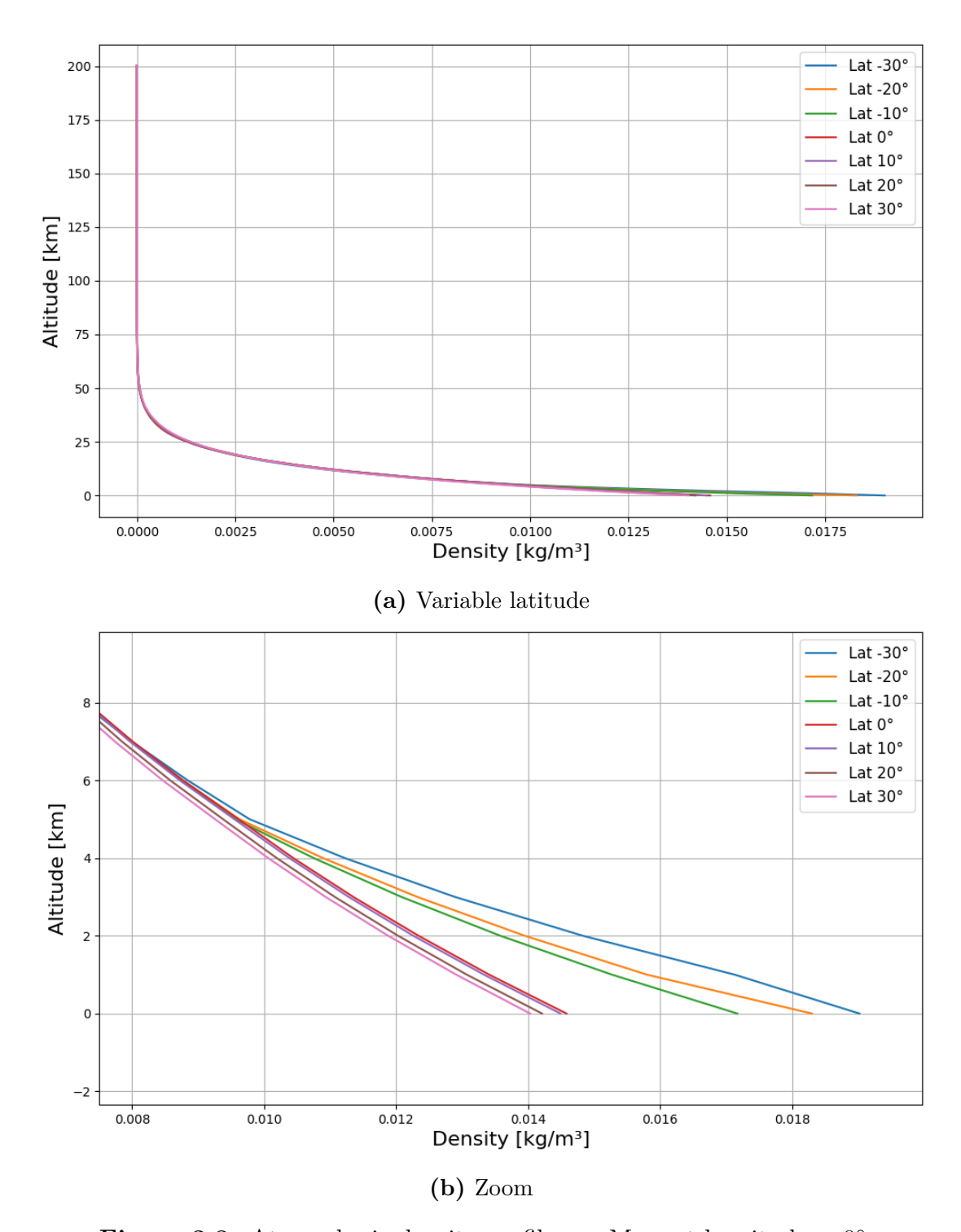


Figure 3.8: Atmospheric density profiles on Mars at longitude =  $0^{\circ}$ 

function of latitude, at a fixed longitude of  $0^{\circ}$  and for different altitudes between 0 km and 140 km.

At ground level (0 km), it can be seen that the southern hemisphere has higher density values, as previously discussed. As altitude increases, density decreases rapidly, as expected from the vertical structure of the Martian atmosphere. Above 60–80 km, the density becomes much lower and the latitudinal variations are less pronounced. Above 100 km, the curves tend to overlap, indicating that at high altitudes, density becomes almost independent of latitude, probably due to the rarefaction of the atmosphere.

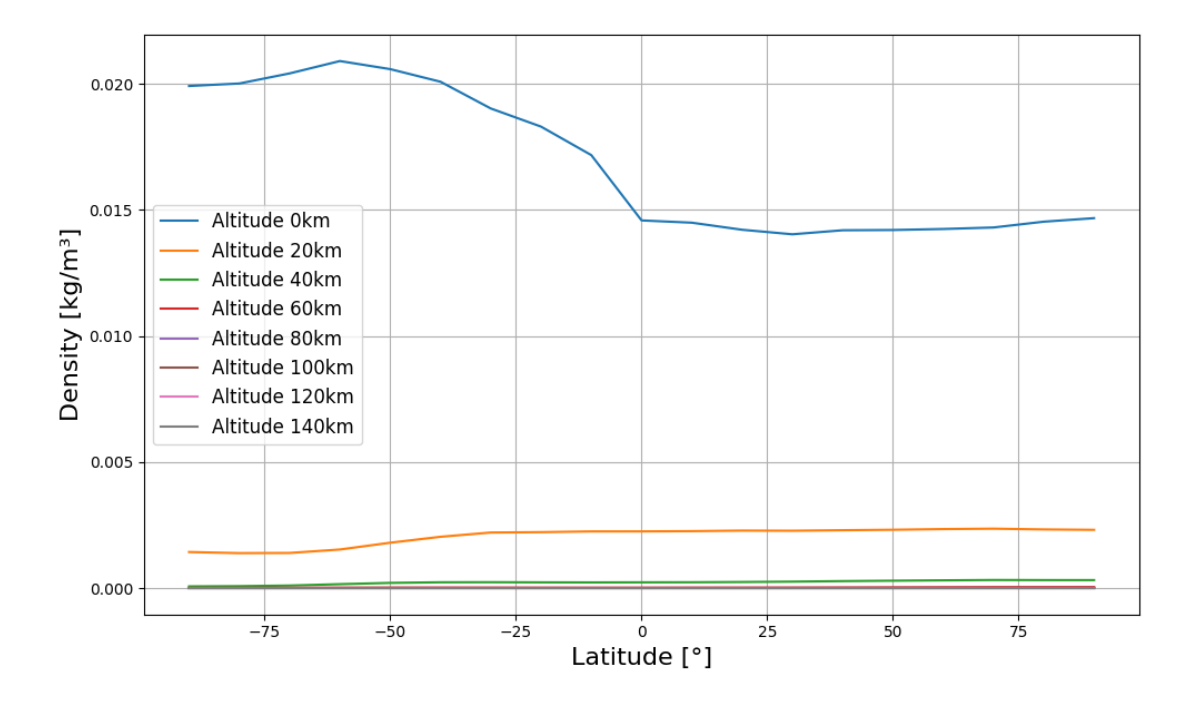


Figure 3.9: Atmospheric density profiles on Mars at longitude =  $0^{\circ}$ 

# Chapter 4

# Optimal Control Problem

The objective of OCP is to find an optimal control strategy to accomplish a given mission. In the context of space exploration, depending on the mission's purpose, different optimisation criteria may be pursued; for example, minimising fuel consumption, thus maximising payload, or minimising the time taken to complete the mission. This implies greater propellant consumption and, therefore, a reduction in payload, unlike the first case, which could require significantly longer mission times. In this thesis, the approach adopted was to maximise payload.

This chapter opens with an introduction dedicated to the main differences between direct and indirect methods, illustrating their respective advantages and disadvantages, and referring to some significant contributions in the literature on this subject. The second section introduces the OCP, starting with the definition of the merit index, and then describing the state variables and boundary conditions (BCs). Next, the formulation of the augmented merit index, necessary to apply the principles of the indirect method, is presented. Next, the transversality and optimality conditions, derived from the analysis of the first variation of the augmented merit index, are discussed, and it is illustrated how the Euler-Lagrange differential equations for the added variables are obtained, together with the algebraic equations that govern the control variables. The third section extends the formulation of the problem to two-point boundary values (TPBVP) to the more general problem of MPBVP. The fourth section is devoted to the presentation of differential correction techniques, with particular reference to single shooting and multiple shooting approaches. Finally, the fifth section describes the application of OCP to the case study considered.

# 4.1 Difference Between Direct and Indirect Numerical Methods

Numerical methods allow a complex and continuous problem, such as the OCP of low-thrust trajectories, to be transformed into a finite set of simpler sub-problems through so-called transcription, which converts ordinary differential equations into a discrete problem.

These methods can be divided into two main categories: direct and indirect. The former, nowadays widely employed thanks to the available computational power, are characterized by greater robustness and simpler implementation, as they transform the continuous problem into a discrete one by discretizing the variables. However, the accuracy of the solutions depends on the grid density, while an excessively fine grid leads to an increase in computational cost, and the numerical result does not always provide a clear analytical interpretation of optimality.

On the other hand, indirect methods (IMs) generally provide more accurate solutions at a lower computational cost, as well as valuable theoretical insights that facilitate understanding and refinement of the solution. However, they also present some practical difficulties, such as high sensitivity to initial conditions, the need for preliminary analytical calculations, and the complexity of the convergence process. Several studies conducted at the Politecnico di Torino have applied OCT to space trajectories [15, 16]. The use of numerical techniques has improved robustness, enabling the application of IMs to increasingly complex scenarios, which historically were addressed almost exclusively with direct methods.

Initially, the indirect approach was applied to TPBVP, and it was later extended to missions involving impulsive manoeuvres [17, 18, 19].

## 4.2 Optimal Control Problem

The OCT aims to maximise a specific merit or functional index, determining the optimal control law that satisfies all the constraints imposed on a trajectory, from the initial state to the final state. The merit index is defined as:

$$\mathcal{J} = \varphi(\vec{x}_0, \vec{x}_f, t_0, t_f) + \int_{t_0}^{t_f} [\Phi(\vec{x}(t), \vec{u}(t), t)] dt$$
 (4.1)

Equation (4.1) consists of two scalar terms: the first,  $\varphi$ , depends on the values assumed by the state variables and the times at the extremes of the interval; the second,  $\Phi$ , is a function of the temporal evolution of the variables.

The merit index can be reformulated as follows:

- the Lagrange formulation, where  $\varphi = 0$
- the Meyer formulation, where  $\Phi = 0$ .

The control problem is described by a set of first-order ordinary differential equations (ODE). These depend on the state vector  $\vec{x}(t) \in \mathbb{R}^n$  and the control vector  $\vec{u}(t) \in \mathbb{R}^m$ , both of which are functions of time. The system of ODE can be written as:

$$\dot{\vec{x}}(t) = \vec{f}(\vec{x}(t), \vec{u}(t), t) \tag{4.2}$$

The BCs may concern the initial or final time and, in this case, are called external conditions. If necessary, additional conditions may be imposed at intermediate instants. The BCs are collected in the constraint vector:

$$\vec{\chi}(\vec{x}_0, \vec{x}_f, t_0, t_f) = 0 \tag{4.3}$$

where  $\vec{\chi}: [\mathbb{R}^n, \mathbb{R}^n, \mathbb{R}, \mathbb{R}] \to \mathbb{R}^q$  contains all the q constraints.

To apply the principles of IM, the optimality conditions are determined by defining an augmented merit function,  $J^*$ , which incorporates both the evolution of the state variables, described by the ODE of the dynamic model, and the degree of compliance with the imposed constraints. Then, the added variables are introduced, collected in the vector  $\vec{\lambda}(t) \in \mathbb{R}^n$ , associated with the state variables, and the Lagrange multipliers,  $\vec{\mu} \in \mathbb{R}^m$ , linked to the boundary conditions. Therefore, the augmented performance index takes the form:

$$\mathcal{J}^* = \varphi + \vec{\mu}^T \vec{\chi} + \int_{t_0}^{t_f} [\Phi + \vec{\lambda}^T (\vec{f} - \dot{\vec{x}})] dt$$
 (4.4)

In the interests of brevity, explicit dependencies on state variables, control variables, and multipliers have been omitted in the previous formulation.

It should be noted that solving the problem using the augmented merit index, (4.4), is mathematically equivalent to the formulation with the standard merit index, (4.1), provided that all the constraints imposed are satisfied.

The introduction of the adjoint variables  $\vec{\lambda}$  and the Lagrange multipliers  $\vec{\mu}$  does not alter the nature of the problem, but allows the optimality conditions to be expressed systematically and manipulated analytically according to the indirect approach.

By integrating by parts the term containing the time derivatives of the state variables, the formulation of equation (4.4) can be simplified, leading to the following expression:

$$\mathcal{J}^* = \varphi + \vec{\mu}^T \vec{\chi} + (\vec{\lambda}_0^T \vec{x}_0 - \vec{\lambda}_f^T \vec{x}_f) + \int_{t_0}^{t_f} [\Phi + \vec{\lambda}^T \vec{f} - \dot{\vec{\lambda}}^T \vec{x}] dt$$
 (4.5)

Within the integral of equation (4.5), there is a central term, the Hamiltonian function, which allows the problem to be reformulated in a form that enables the conditions of optimality to be derived systematically according to PMP.

$$\mathcal{H} \triangleq \Phi + \vec{\lambda}^T \vec{f}. \tag{4.6}$$

### 4.2.1 Boundary conditions for optimality

To determine the optimality conditions, it is necessary to extremise the augmented merit index  $\mathcal{J}^*$ . Therefore, the variation of the functional is calculated by deriving with respect to each of the variables present and imposing that this variation be zero. In particular, one looks for the values of the adjoint variables  $\vec{\lambda}$  and Lagrange multipliers  $\vec{\mu}$  for which  $\delta \mathcal{J}^* = 0$ . After appropriate algebraic steps, the following expression of the first derivative of  $\mathcal{J}^*$  is obtained:

$$\delta \mathcal{J}^* = \left(\frac{\partial \varphi}{\partial t_0} + \vec{\mu}^T \frac{\partial \vec{\chi}}{\partial t_0} - \mathcal{H}_0\right) \delta t_0 \tag{4.7a}$$

$$+ \left( \frac{\partial \varphi}{\partial t_f} + \vec{\mu}^T \frac{\partial \vec{\chi}}{\partial t_f} + \mathcal{H}_f \right) \delta t_f \tag{4.7b}$$

$$+ \left( \frac{\partial \varphi}{\partial \vec{x}_0} + \vec{\mu}^T \frac{\partial \vec{\chi}}{\partial \vec{x}_0} + \vec{\lambda}_0^T \right) \delta \vec{x}_0 \tag{4.7c}$$

$$+ \left( \frac{\partial \varphi}{\partial \vec{x}_f} + \vec{\mu}^T \frac{\partial \vec{\chi}}{\partial \vec{x}_f} - \vec{\lambda}_f^T \right) \delta \vec{x}_f \tag{4.7d}$$

$$+ \int_{t_0}^{t_f} \left[ \left( \frac{\partial \mathcal{H}}{\partial \vec{x}} + \dot{\vec{\lambda}}^T \right) \delta \vec{x} + \frac{\partial \mathcal{H}}{\partial \vec{u}} \delta \vec{u} \right] dt$$
 (4.7e)

From equation (4.7), two transversality conditions are obtained, associated with the initial and final instants, obtained by imposing the cancellation of expressions (4.7a) and (4.7b), and a set of 2n optimality conditions, relating to the state variables at the extreme points, resulting from the cancellation of equations (4.7c) and (4.7d). As regards transversality, if time does not appear in either the cost function  $\varphi$  or the constraints  $\vec{\chi}$ , the Hamiltonian  $\mathcal{H}$  is zero at the initial and final instants, and the time values are determined by the optimisation process. Conversely, if time is constrained (initial and/or final), the corresponding value of the Hamiltonian takes on a value other than zero and is in turn subject to optimisation.

A similar reasoning applies to the optimality conditions: if a state variable  $x_i$  does not appear in either the function  $\varphi$  or in the function  $\vec{\chi}$ , the corresponding added variable  $\lambda_{x_i}$  is zero.

### 4.2.2 Adjoint and control variables

From the annulment of the coefficients in expression (4.7e), two fundamental results are obtained. In particular, by imposing the annulment of the coefficient associated with  $\delta \vec{x}$ , it is possible to obtain a system of n Euler-Lagrange differential equations for the added variables, whose explicit formulation is given in Appendix C.

$$\dot{\vec{\lambda}} = -\left(\frac{\delta \mathcal{H}}{\delta \vec{x}}\right)^T \tag{4.8}$$

The added variables are uniquely associated with the corresponding state variables; consequently,  $\dot{\vec{\lambda}} \in \mathbb{R}^n$ .

Similarly, by imposing the annulment of the coefficient of the term  $\delta \vec{u}$ , it is possible to obtain a set of m algebraic equations for the control variables:

$$\left(\frac{\delta \mathcal{H}}{\delta \vec{u}}\right)^T = 0 
\tag{4.9}$$

When bounds are imposed on the control, for example  $u_{min} \leq u \leq u_{max}$ , equation (4.9) cannot always be satisfied. This occurs in particular when the Hamiltonian is linear or affine with respect to the control: in such cases, the derivative  $\delta \mathcal{H}/\delta u$  is constant and cannot vanish except in special situations (e.g., when the constant is zero).

In these circumstances, the problem is solved by letting the control take one of the admissible extreme values:

- if the coefficient in front of the control is positive, the optimal control is  $u = u_{max}$ ;
- if it is negative, the optimal control is  $u = u_{min}$ .

This strategy is known as bang-bang control, as control switches instantly between the two limit values without assuming intermediate values. In the case discussed in this thesis, this applies to the thrust T, which is linear in the Hamiltonian: the optimal profile is therefore characterised by intervals in which the thrust is maximum  $(T = T_{max})$  alternating with intervals in which it is zero  $(T = T_{min})$ . A special case occurs if the coefficient of the derivative with respect to the control is zero  $(k_u = 0)$  for a finite time interval. In this situation, the control is not determined by bang-bang logic, but by a different strategy, called singular arc. These cases require specific analysis (described, for example, in [20]), but they do not arise in the context of this thesis and will therefore not be discussed.

## 4.3 Multi-Point Optimal Control Problem

A MPBVP is a generalisation of the TPBVP. It occurs when, in addition to the constraints imposed at the ends of the trajectory, conditions are also specified at internal points.

To deal with this type of problem, the trajectory is divided into  $n_p$  sub-intervals, called phases or arcs, a solution that improves the robustness of the numerical code and facilitates convergence.

Within each arc, the variables evolve continuously, while discontinuities may occur at the internal boundaries (i.e., at the junctions between consecutive arcs). The duration of each arc is generally unknown and constitutes an optimisation variable, potentially different from arc to arc. The BCs can be imposed not only at the global extremes of the time interval, but also at the internal boundaries. These conditions may depend on both the state variables and the independent variable time.

Figure 4.1 (taken from [8]) shows a schematic representation of a MPBVP, composed of  $n_p$  arcs. It highlights how the j-th arc begins at  $t_{(j-1)_+}$  and ends at  $t_{j_-}$ , with boundary states  $\vec{x}_{(j-1)_+}$  and  $\vec{x}_{j_-}$ , respectively.

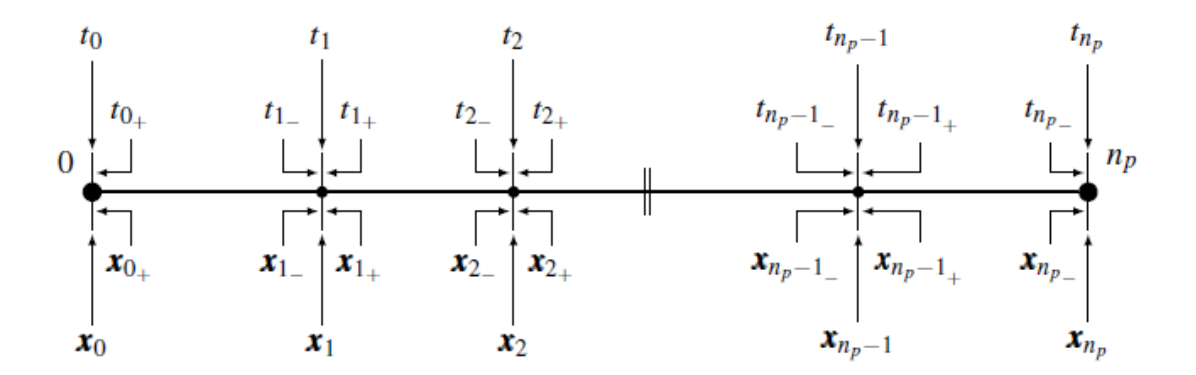


Figure 4.1: Schematic representation of a MPBVP

The main formulations relating to MPBVP are given below. In particular, the constraint conditions can be expressed in the following form:

$$\vec{\chi}(\vec{x}_{(j-1)+}, \vec{x}_{j-}, t_{(j-1)+}, t_{j-}) = 0, \qquad j = 1, \dots, n_p.$$
(4.10)

The merit index is instead defined as:

$$\mathcal{J} = \varphi\left(\vec{x}_{(j-1)_{+}}, \vec{x}_{j_{-}}, t_{(j-1)_{+}}, t_{j_{-}}\right) + \sum_{j=1}^{n_{p}} \int_{t_{(j-1)_{+}}}^{t_{j_{-}}} \Phi\left(\vec{x}(t), \vec{u}(t), t\right) dt. \tag{4.11}$$

After integration by parts, the augmented functional takes the following form:

$$\mathcal{J}^* = \varphi + \vec{\mu}^T \vec{\chi} + \sum_{j=1}^{n_p} \left( \vec{\lambda}_{(j-1)_+}^T \vec{x}_{(j-1)_+} - \vec{\lambda}_{j_-}^T \vec{x}_{j_-} \right) + \sum_{j=1}^{n_p} \int_{t_{(j-1)_+}}^{t_{j_-}} \left( \Phi + \vec{\lambda}^T \vec{f} - \dot{\vec{\lambda}}^T \vec{x} \right) dt.$$

$$(4.12)$$

The first order differentiation  $\delta \mathcal{J}^*$  now is expressed per each arc as:

$$\delta \mathcal{J}^* = \left(\frac{\partial \varphi}{\partial t_{(j-1)_+}} + \vec{\mu}^T \frac{\partial \vec{\chi}}{\partial t_{(j-1)_+}} - \mathcal{H}_{(j-1)_+}\right) \delta t_{(j-1)_+}$$
(4.13a)

$$+ \left( \frac{\partial \varphi}{\partial t_{j_{-}}} + \vec{\mu}^{T} \frac{\partial \vec{\chi}}{\partial t_{j_{-}}} + \mathcal{H}_{j_{-}} \right) \delta t_{j_{-}}$$

$$(4.13b)$$

$$+ \left( \frac{\partial \varphi}{\partial \vec{x}_{(j-1)_{+}}} + \vec{\mu}^{T} \frac{\partial \vec{\chi}}{\partial \vec{x}_{(j-1)_{+}}} + \vec{\lambda}_{(j-1)_{+}}^{T} \right) \delta \vec{x}_{(j-1)_{+}}$$

$$(4.13c)$$

$$+ \left( \frac{\partial \varphi}{\partial \vec{x}_{j_{-}}} + \vec{\mu}^{T} \frac{\partial \vec{\chi}}{\partial \vec{x}_{j_{-}}} - \vec{\lambda}_{j_{-}}^{T} \right) \delta \vec{x}_{j_{-}}$$

$$(4.13d)$$

$$+\sum_{j=1}^{n_p} \int_{t_{(j-1)_+}}^{t_{j_-}} \left[ \left( \frac{\partial \mathcal{H}}{\partial \vec{x}} + \dot{\vec{\lambda}} \right) \delta \vec{x} + \frac{\partial \mathcal{H}}{\partial \vec{u}} \delta \vec{u} \right] dt, \qquad j = 1, \dots, n_p.$$
 (4.13e)

### 4.4 Differential Correction

Differential correction is a numerical technique used to determine trajectories that satisfy pre-established constraints on the final state, starting from an approximate initial hypothesis. The central idea is that the final state of a trajectory depends sensitively on the initial conditions: small variations in the initial state are reflected in variations in the final state. Understanding this relationship allows targeted corrections to be introduced to progressively reduce the gap between the obtained state and the desired state.

Figure 4.2 shows the application of the *single shooting* procedure to a Hohmann transfer. The correct trajectory with desired initial conditions  $\tilde{\vec{X}}^*(\tau_0)$  is shown in grey, connecting an orbit with a dimensionless altitude of 2.5 to a lower orbit with a radius of 1.5. In black, on the other hand, is a transfer obtained from approximate initial conditions  $\tilde{\vec{X}}(\tau_0)$ : in this case, the manoeuvre ends at a point  $\tilde{\vec{X}}(\tilde{\vec{X}}(\tau_0), \tau_f)$  that differs from the correct one  $\tilde{\vec{X}}^*(\tilde{\vec{X}}^*(\tau_0), \tau_f)$ . The initial points coincide in position space, so the deviation is attributable to an error in the initial velocities. Knowing the desired final state and the state actually obtained, the variation between the two can be defined as:

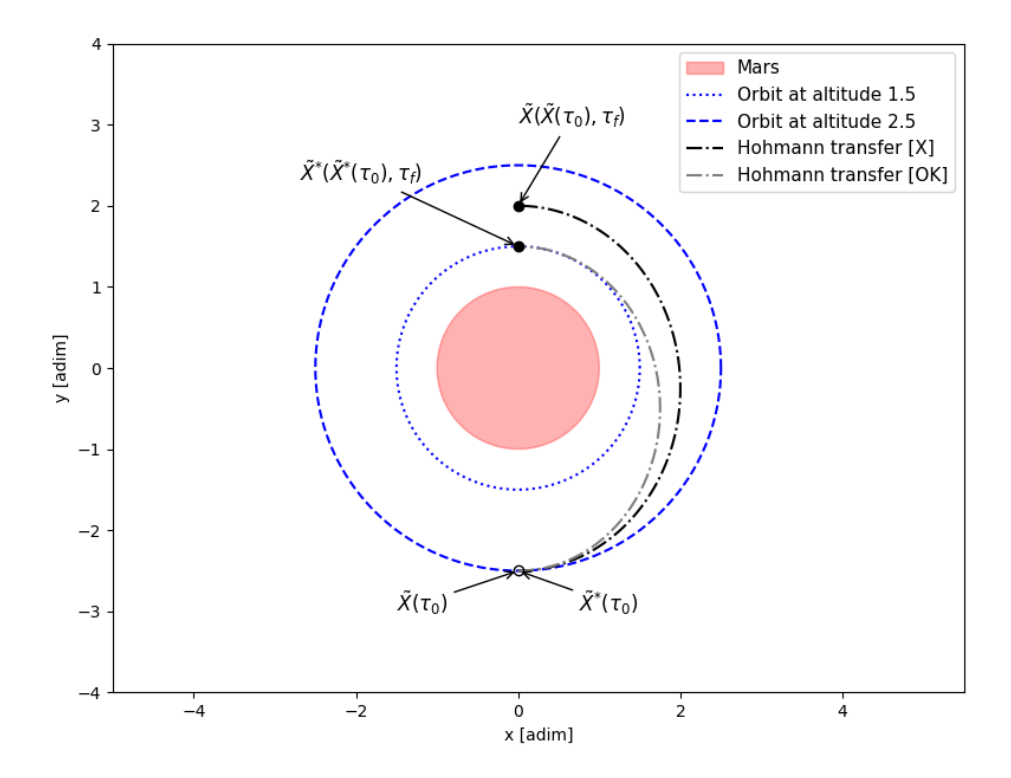


Figure 4.2: Single shooting differential correction procedure from a generic state  $\tilde{\vec{X}}$  to a desired reference state  $\tilde{\vec{X}}^*$  for a Hohmann transfer

$$\delta \tilde{\vec{X}}(\tau_f) = \tilde{\vec{X}}(\tilde{\vec{X}}(\tau_0), \ \tau_f) - \tilde{\vec{X}}^*(\tilde{\vec{X}}^*(\tau_0), \ \tau_f)$$

$$(4.14)$$

To progressively reduce this difference, it is necessary to introduce a correction in the initial state:

$$\tilde{\vec{X}}^*(\tau_0) = \tilde{\vec{X}}(\tau_0) + \delta \tilde{\vec{X}}(\tau_0)$$
(4.15)

By combining the two relations, the variation in the final state can be expressed as:

$$\delta \tilde{\vec{X}}(\tau_f) = \tilde{\vec{X}}(\tilde{\vec{X}}(\tau_0), \tau_f) - \tilde{\vec{X}}^*(\tilde{\vec{X}}^*(\tau_0), \tau_f)$$

$$= \tilde{\vec{X}}(\tilde{\vec{X}}(\tau_0), \tau_f) - \tilde{\vec{X}}^*(\tilde{\vec{X}}(\tau_0) + \delta \tilde{\vec{X}}(\tau_0), \tau_f)$$

$$= \frac{\partial \tilde{\vec{X}}(\tau_f)}{\partial \tilde{\vec{X}}(\tau_0)} \delta \tilde{\vec{X}}(\tau_0)$$

$$\delta \tilde{\vec{X}}(\tau_f) = \tilde{\Phi}(\tau_f, \tau_0) \delta \tilde{\vec{X}}(\tau_0). \tag{4.16}$$

where  $\tilde{\Phi}(\tau_f, \tau_0)$  is the *State Transition Matrix* (STM), which represents the linear mapping between perturbations of the initial state and variations in the final state.

The STM evolves along the trajectory according to a linear differential equation involving the partial derivatives of the dynamical field, collected in a Jacobian matrix  $\tilde{A}(\tau)$ .

$$\tilde{A}(\tau) = \begin{bmatrix} \frac{\partial \vec{x}}{\partial \vec{x}} & \frac{\partial \vec{x}}{\partial \vec{\lambda}} \\ \frac{\partial \vec{\lambda}}{\partial \vec{x}} & \frac{\partial \vec{\lambda}}{\partial \vec{\lambda}} \end{bmatrix} = \begin{bmatrix} \tilde{A}_{\vec{x}\vec{x}} & \tilde{A}_{\vec{x}\vec{\lambda}} \\ \tilde{A}_{\vec{\lambda}\vec{x}} & \tilde{A}_{\vec{\lambda}\vec{\lambda}} \end{bmatrix}. \tag{4.17}$$

Its integration, carried out in parallel with that of the equations of motion, allows the sensitivity of the state with respect to the initial conditions to be evaluated at any moment. In spherical coordinates, the STM takes the form:

$$\tilde{\Phi}(\tau, \tau_{0}) = \begin{bmatrix}
\frac{\partial r}{\partial r_{0}} & \frac{\partial r}{\partial \vartheta_{0}} & \frac{\partial r}{\partial \varphi_{0}} & \frac{\partial r}{\partial u_{0}} & \frac{\partial r}{\partial v_{0}} & \frac{\partial r}{\partial w_{0}} \\
\frac{\partial \vartheta}{\partial r_{0}} & \frac{\partial \vartheta}{\partial \vartheta_{0}} & \frac{\partial \vartheta}{\partial \varphi_{0}} & \frac{\partial \vartheta}{\partial u_{0}} & \frac{\partial \vartheta}{\partial v_{0}} & \frac{\partial \vartheta}{\partial w_{0}} \\
\frac{\partial \varphi}{\partial r_{0}} & \frac{\partial \varphi}{\partial \vartheta_{0}} & \frac{\partial \varphi}{\partial \varphi_{0}} & \frac{\partial \varphi}{\partial u_{0}} & \frac{\partial \varphi}{\partial v_{0}} & \frac{\partial \varphi}{\partial w_{0}} \\
\frac{\partial u}{\partial r_{0}} & \frac{\partial u}{\partial \vartheta_{0}} & \frac{\partial u}{\partial \varphi_{0}} & \frac{\partial u}{\partial u_{0}} & \frac{\partial u}{\partial v_{0}} & \frac{\partial u}{\partial w_{0}} \\
\frac{\partial v}{\partial r_{0}} & \frac{\partial v}{\partial \vartheta_{0}} & \frac{\partial v}{\partial \varphi_{0}} & \frac{\partial v}{\partial u_{0}} & \frac{\partial v}{\partial v_{0}} & \frac{\partial v}{\partial w_{0}} \\
\frac{\partial w}{\partial r_{0}} & \frac{\partial w}{\partial \vartheta_{0}} & \frac{\partial w}{\partial \varphi_{0}} & \frac{\partial w}{\partial u_{0}} & \frac{\partial w}{\partial v_{0}} & \frac{\partial w}{\partial w_{0}} \\
\frac{\partial w}{\partial r_{0}} & \frac{\partial w}{\partial \vartheta_{0}} & \frac{\partial w}{\partial \varphi_{0}} & \frac{\partial w}{\partial u_{0}} & \frac{\partial w}{\partial v_{0}} & \frac{\partial w}{\partial w_{0}}
\end{bmatrix} (4.18)$$

As shown in the final part of equation (4.18), the matrix is expressed in compact form as consisting of four square  $3 \times 3$  sub-matrices. These represent the partial

derivatives of positions with respect to positions  $(\tilde{\Phi}_{pp})$ , positions with respect to velocities  $(\tilde{\Phi}_{pv})$ , velocities with respect to positions  $(\tilde{\Phi}_{vp})$ , and velocities with respect to velocities  $(\tilde{\Phi}_{vv})$ .

Finally, the time evolution of the STM is described by the following differential relation:

$$\dot{\tilde{\Phi}}(\tau, \tau_0) = \frac{d}{d\tau} \tilde{\Phi}(\tau, \tau_0) = \frac{d}{d\tau} \left( \frac{\partial \tilde{\vec{X}}}{\partial \tilde{\vec{X}}_0} \right)$$

$$= \frac{\partial}{\partial \tilde{\vec{X}}_0} \left( \frac{d\tilde{\vec{X}}}{d\tau} \right)$$

$$= \frac{\partial \dot{\tilde{\vec{X}}}}{\partial \tilde{\vec{X}}} \frac{\partial \tilde{\vec{X}}}{\partial \tilde{\vec{X}}_0},$$

$$\dot{\tilde{\Phi}}(\tau, \tau_0) = \tilde{A}(\tau) \, \tilde{\Phi}(\tau, \tau_0) \tag{4.19}$$

### 4.4.1 Single shooting

The single shooting procedure consists in properly adjusting the initial conditions of a trajectory so that the final state satisfies a prescribed set of constraints. The idea is that, given an approximate initial state, the obtained trajectory does not exactly reach the desired state; through iterative corrections of the initial conditions, the final discrepancy is progressively reduced.

As shown in Figure 4.2, the difference between the two final states is mainly due to the initial velocities; therefore, only these must be left free to vary in the correction, while keeping the position variables fixed.

Therefore, the free-variable vector,  $\tilde{\vec{X}}_0 \in \mathbb{R}^{n \times 1}$ , is defined as:

$$\tilde{\vec{X}}_0 = \{X_1, X_2, ..., X_n\}^T \tag{4.20}$$

and may contain components of position, velocity, and integration time.

On the other hand, the constraint vector,  $\vec{\chi}(\vec{X}_f) \in \mathbb{R}^{m \times 1}$ , which represents the difference between the obtained final state and the desired one, is expressed as:

$$\vec{\chi}(\tilde{\vec{X}}_f) = \{\chi_1, \chi_2, \dots, \chi_m\}^T = \begin{cases} \xi - \xi^* \\ \eta - \eta^* \\ \zeta - \zeta^* \\ \dot{\xi} - \dot{\xi}^* \\ \dot{\eta} - \dot{\eta}^* \\ \dot{\zeta} - \dot{\zeta}^* \end{cases}$$
(4.21)

The goal is to find  $\tilde{\vec{X}}_0^*$  such that  $\vec{\chi}(\tilde{\vec{X}}_f^*) = 0$ . To linearize the problem, a first-order Taylor expansion of the constraint vector around the current estimate  $\vec{X}_0$  is performed:

$$\vec{\chi}(\tilde{\vec{X}}) \approx \vec{\chi}(\tilde{\vec{X}}_0) + \frac{\partial \vec{\chi}(\tilde{\vec{X}}_0)}{\partial \tilde{\vec{X}}}(\tilde{\vec{X}} - \tilde{\vec{X}}_0).$$
 (4.22)

where the matrix of partial derivatives represents the Jacobian of the constraints:

$$\frac{\partial \chi(\tilde{X}_0)}{\partial \tilde{X}} = \tilde{J}\left(\chi(\tilde{X}_0), \tilde{X}\right) = \begin{bmatrix}
\frac{\partial \chi_1}{\partial \tilde{X}_1} & \frac{\partial \chi_1}{\partial \tilde{X}_2} & \cdots & \frac{\partial \chi_1}{\partial \tilde{X}_n} \\
\frac{\partial \chi_2}{\partial \tilde{X}_1} & \frac{\partial \chi_2}{\partial \tilde{X}_2} & \cdots & \frac{\partial \chi_2}{\partial \tilde{X}_n} \\
\vdots & \vdots & \ddots & \vdots \\
\frac{\partial \chi_m}{\partial \tilde{X}_1} & \frac{\partial \chi_m}{\partial \tilde{X}_2} & \cdots & \frac{\partial \chi_m}{\partial \tilde{X}_n}
\end{bmatrix}.$$
(4.23)

The method is iterative: starting from an initial guess, the residual  $\chi_r$  at iteration r is computed and a correction is applied using the Jacobian. The relation takes the form:

$$\chi_{r+1} = \chi_r + J(\chi_r) \left( \tilde{\vec{X}}_{r+1} - \tilde{\vec{X}}_r \right). \tag{4.24}$$

To satisfy the constraint, it must hold that  $\chi_{r+1} = 0$ , from which follows the update rule:

$$\tilde{\vec{X}}_{r+1} = \tilde{\vec{X}}_r - J(\chi_r)^{-1} \chi_r. \tag{4.25}$$

If the number of variables is greater than the number of constraints (n > m), the minimum-norm solution is used:

$$\tilde{\vec{X}}_{r+1} = \tilde{\vec{X}}_r - \left[ J(\chi_r)^T J(\chi_r) \right]^{-1} J(\chi_r)^T \chi_r.$$
 (4.26)

To improve numerical stability, a relaxation factor  $\kappa_R$  can be introduced, which reduces the magnitude of corrections at each iteration.

### 4.4.2 Multiple shooting

When the trajectory is long, sensitive to initial conditions or composed of distinct segments (e.g. propulsive arcs and free flight sections), the single shooting method may not be robust enough. In such cases, multiple shooting is used, which divides the trajectory into several segments. Each segment is integrated starting from assumed conditions, and differential correction imposes continuity constraints at the junctions between segments. This reduces propagation errors and improves convergence.

#### 4.4.3 Variable-time vs fixed-time

In the case of free-time problems, the state vector also includes the integration time, which in the following case study represents the engine burn time and the coasting duration. Therefore, the state vector becomes:

$$\tilde{\vec{X}}_0 = \{ r \ \vartheta \ \varphi \ u \ v \ w \ \tau \}^T \tag{4.27}$$

The constraint vector coincides with that in equation (4.21), so the Jacobian matrix introduces an additional column into the Jacobian of equation (4.23), making  $\tilde{J} \in \mathbb{R}^{6 \times 7}$ . It takes the form:

$$\tilde{J}(\vec{\chi}(\tilde{X}_0), \tilde{X}_f) = \begin{bmatrix}
\frac{\partial r_f}{\partial r_0} & \frac{\partial r_f}{\partial \theta_0} & \frac{\partial r_f}{\partial \varphi_0} & \frac{\partial r_f}{\partial u_0} & \frac{\partial r_f}{\partial v_0} & \frac{\partial r_f}{\partial w_0} & \frac{\partial r_f}{\partial \tau} \\
\frac{\partial \theta_f}{\partial r_0} & \frac{\partial \theta_f}{\partial \theta_0} & \frac{\partial \theta_f}{\partial \varphi_0} & \frac{\partial \theta_f}{\partial u_0} & \frac{\partial \theta_f}{\partial v_0} & \frac{\partial \theta_f}{\partial w_0} & \frac{\partial \theta_f}{\partial \tau} \\
\frac{\partial \varphi_f}{\partial r_0} & \frac{\partial \varphi_f}{\partial \theta_0} & \frac{\partial \varphi_f}{\partial \varphi_0} & \frac{\partial \varphi_f}{\partial u_0} & \frac{\partial \varphi_f}{\partial v_0} & \frac{\partial \varphi_f}{\partial w_0} & \frac{\partial \varphi_f}{\partial \tau} \\
\frac{\partial u_f}{\partial r_0} & \frac{\partial u_f}{\partial \theta_0} & \frac{\partial u_f}{\partial \varphi_0} & \frac{\partial u_f}{\partial u_0} & \frac{\partial u_f}{\partial v_0} & \frac{\partial u_f}{\partial w_0} & \frac{\partial u_f}{\partial \tau} \\
\frac{\partial v_f}{\partial r_0} & \frac{\partial v_f}{\partial \theta_0} & \frac{\partial v_f}{\partial \varphi_0} & \frac{\partial v_f}{\partial u_0} & \frac{\partial v_f}{\partial v_0} & \frac{\partial v_f}{\partial w_0} & \frac{\partial v_f}{\partial \tau} \\
\frac{\partial w_f}{\partial r_0} & \frac{\partial w_f}{\partial \theta_0} & \frac{\partial w_f}{\partial \varphi_0} & \frac{\partial w_f}{\partial u_0} & \frac{\partial w_f}{\partial v_0} & \frac{\partial w_f}{\partial w_0} & \frac{\partial w_f}{\partial \tau} \\
\frac{\partial w_f}{\partial r_0} & \frac{\partial w_f}{\partial \theta_0} & \frac{\partial w_f}{\partial \varphi_0} & \frac{\partial w_f}{\partial u_0} & \frac{\partial w_f}{\partial v_0} & \frac{\partial w_f}{\partial w_0} & \frac{\partial w_f}{\partial \tau}
\end{bmatrix} (4.28)$$

This correction approach is known as the variable-time shooting method and takes into account not only the evolution of the state but also the effect of the

integration time on the final state. In the literature, it is referred to as Variable-Time Differential Correction (VTDC). If the integration time is not treated as a free variable, the Jacobian coincides entirely with the STM, and the procedure is called fixed-time correction, or Fixed-Time Differential Correction (FTDC).

## 4.5 Application of OCP to the Case Study

The application of OCT to the case study considers the maximisation of final mass, or the minimisation of propellant consumption, as its objective. This objective is represented by the merit index, expressed as a function of the control law vector  $\vec{u} = \vec{T}$  and the following state variables:

$$\vec{x} = \{r \ \theta \ \varphi \ u \ v \ w \ m\}^T \tag{4.29}$$

with  $\vec{x} \in \mathbb{R}^n$ , where each state variable is associated with an adjoint variable, or costate, collectively defined in  $\vec{y} \in \mathbb{R}^{2n}$  as:

$$\vec{y} = \{ r \ \theta \ \varphi \ u \ v \ m \ \lambda_r \ \lambda_{\theta} \ \lambda_{\varphi} \ \lambda_u \ \lambda_v \ \lambda_w \ \lambda_m \}^T.$$
 (4.30)

The system of ODEs describing the dynamics of the satellite introduced in section 2.4.2:

$$\begin{cases} \frac{dr}{dt} = u \\ \frac{d\vartheta}{dt} = \frac{v}{r\cos\varphi} \\ \frac{d\varphi}{dt} = \frac{w}{r} \\ \frac{du}{dt} = -\frac{\mu}{r^2} + \frac{v^2}{r} + \frac{w^2}{r} + \frac{T_u}{m} + (a_p)_u \\ \frac{dv}{dt} = -\frac{uv}{r} + \frac{vw}{r}\tan\varphi + \frac{T_v}{m} + (a_p)_v \\ \frac{dw}{dt} = -\frac{uw}{r} - \frac{v^2}{r}\tan\varphi + \frac{T_w}{m} + (a_p)_w \\ \frac{dm}{dt} = -\frac{T}{c} \end{cases}$$

$$(4.31)$$

From this system of equations, the Hamiltonian function can be defined as:

$$\mathcal{H} = \vec{\lambda}^T \vec{f} = \sum_{i=1}^{2n} \lambda_i f_i \tag{4.32}$$

which, once expanded and highlighting the terms dependent on the thrust T, takes the form:

$$H = \lambda_r u + \lambda_{\vartheta} \frac{v}{r \cos \varphi} \lambda_{\varphi} \frac{w}{r}$$

$$+ \lambda_u \left[ -\frac{\mu}{r^2} + \frac{v^2}{r} + \frac{w^2}{r} + (a_p)_u \right]$$

$$+ \lambda_v \left[ -\frac{uv}{r} + \frac{wv}{r} tan\varphi + (a_p)_v \right]$$

$$+ \lambda_w \left[ -\frac{uw}{r} - \frac{v^2}{r} tan\varphi + (a_p)_w \right]$$

$$+ \frac{T}{m} \left( \lambda_V^T \frac{\vec{T}}{T} - \lambda_m \frac{m}{c} \right), \qquad (4.33)$$

where  $\vec{\lambda_V}$  represents the *primer vector*, defined as  $\lambda_V = \sqrt{\lambda_u^2 + \lambda_v^2 + \lambda_w^2}$ . From this formulation, the *switching function*,  $\mathcal{S}_{\mathcal{F}}$ , emerges:

$$S_{\mathcal{F}} = \lambda_V^{\vec{T}} \frac{\vec{T}}{T} - \lambda_m \frac{m}{c}. \tag{4.34}$$

Knowing the value of the switching function, according to the bang-bang control theory (see Section 4.2.2), we can obtain the optimal value of thrust T:

$$T = \begin{cases} 0 & if \ \mathcal{S}_{\mathcal{F}} < 0 \\ T_{MAX} & if \ \mathcal{S}_{\mathcal{F}} > 0 \end{cases}$$
 (4.35)

The thrust vector  $\vec{T}$  is defined by the *elevation angle*,  $\alpha_T$ , and the *heading angle*,  $\beta_T$ , which determine the in-plane and out-of-plane thrust components, respectively:

$$\vec{T} = \begin{cases} T_u \\ T_v \\ T_w \end{cases} = T \begin{cases} \sin \alpha_T \\ \cos \alpha_T \cos \beta_T \\ \cos \alpha_T \sin \beta_T \end{cases}$$
 (4.36)

To determine the optimal value of the thrust angles, the Hamiltonian function (4.33) is derived with respect to these variables:

$$\frac{\partial \mathcal{H}}{\partial \alpha_T} = 0 = \lambda_v \cos \alpha_T - (\lambda_u \cos \beta_T + \lambda_w \sin \beta_T) \sin \alpha_T \tag{4.37a}$$

$$\frac{\partial \mathcal{H}}{\partial \beta_T} = 0 = -\lambda_u \sin \beta_T + \lambda_w \cos \beta_T \tag{4.37b}$$

The solution of system (4.37) leads to the following relations:

$$\sin \alpha_T = \frac{\lambda_u}{\lambda_v} \tag{4.38a}$$

$$\cos \alpha_T \cos \beta_T = \frac{\lambda_v}{\lambda_v} \tag{4.38b}$$

$$\cos \alpha_T \sin \beta_T = \frac{\lambda_w}{\lambda_v} \tag{4.38c}$$

These values correspond to the cosines of the  $primer\ vector$  and coincide with the components of the thrust vector already introduced in equation (4.36).

## Chapter 5

# Results

The purpose of this chapter is to present and analyse the results obtained from numerical simulations developed in Python, aimed at studying a controlled descent strategy on Mars.

The vehicle considered has an initial mass of 600 kg, a wet surface area of 2 m<sup>2</sup> and an aerodynamic drag coefficient of  $C_D = 2.2$ . It is equipped with two propulsion systems: an ion thruster, with an effective exhaust velocity of 40,000 m/s and a thrust of 0.05 N, used in the initial orbital phases, and a chemical thruster, with an effective exhaust velocity of 4,500 m/s and maximum thrust of 300,000 N, intended for the final docking phase.

The mission profile envisages an initial phase in which the vehicle departs from a circular orbit at an altitude of 140 km, characterised by tangential velocity alone, and progressively reduces its altitude using the ion thruster. The propulsive action, combined with atmospheric resistance, induces the transition from circular to elliptical orbit. After each intervention, the orbit is left to evolve for two orbital periods in free propagation, so as to allow the thruster to cool down before the next ignition. This process is repeated until atmospheric drag becomes dominant and leads to the decay of the orbit.

Once an altitude of 15 km is reached, a parachute is opened which, by exploiting aerodynamic drag, further reduces the vehicle's speed. Finally, near the surface, the chemical thruster is ignited, ensuring a controlled and precise landing.

To simplify the numerical analysis, a dimensionless approach was adopted to avoid dealing with very large quantities. The altitude was scaled using the radius of Mars  $R_{\sigma} = 3396$  km, while the velocities u, v, w and the effective exhaust velocity were normalised with respect to the orbital velocity at the planet's surface, equal

to  $v_{\sigma} = \sqrt{\mu_{\sigma}/R_{\sigma}} = 3.551$  km/s. Time was dimensionless using the parameter  $T = R_{\sigma}/v_{\sigma}$ , while the mass of the satellite was set as the reference unit. The characteristic acceleration  $a = v_{\sigma}^2/R_{\sigma}$  was used as a parameter to render derived quantities dimensionless, such as thrust, expressed with respect to the product of the satellite's mass and the characteristic acceleration. In general, all other quantities were made dimensionless using appropriate combinations of these fundamental parameters, ensuring consistency and simplicity in the interpretation of the results.

The following sections are organised in such a way as to first describe the manoeuvres and propagation phases obtained with the ion thruster, then the descent with parachutes and finally the terminal phase with the use of the chemical thruster, up to landing.

To execute the algorithm implemented in Python, a Graphical User Interface (GUI) was developed with the valuable support of supervisor Luigi Mascolo, as shown in Figure 5.1. This tool made it possible to visualise and analyse the behaviour of the state variables as the initial conditions of the added variables varied, as well as the switch times and the final time, thus facilitating the understanding and validation of the results obtained.

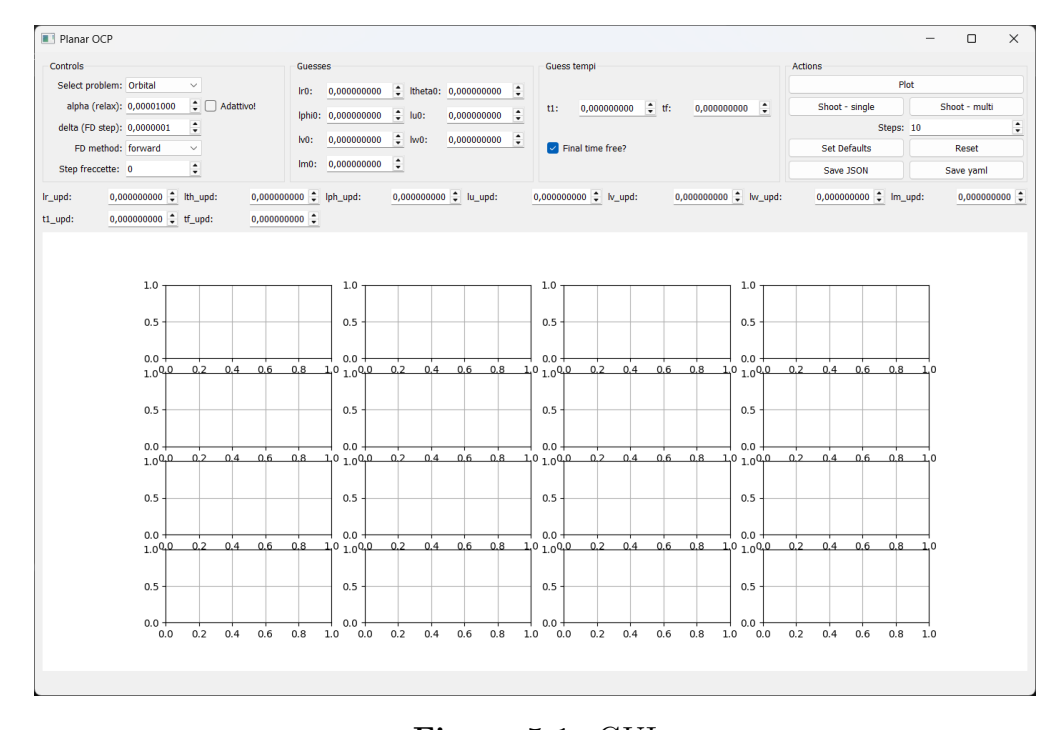


Figure 5.1: GUI

#### 5.1 Ion Thrusters

Figure 5.2 shows the evolution of the state variables and the corresponding added variables during the first manoeuvre. In the graphs, the orange line identifies the interval in which the electric thrusters are on, while the blue line corresponds to the coasting phase, in which no thrust is applied. The manoeuvres performed with the electric thruster all have the same structure, characterised by the alternation between an ignition phase and a shutdown phase. Table 5.1 shows the dimensionless initial conditions, while Table 5.2 shows the initial conditions of the added variables, including the switching times and the final time calculated to ensure the convergence of the solution.

r	$\vartheta$	arphi	$\boldsymbol{u}$	$oldsymbol{v}$	w	m
1.0412249705535925	0.0	0.0	0.0	0.980003693778245	0.0	1.0

**Table 5.1:** Initial state for the first manoeuvre

$oldsymbol{\lambda_r}$	$oldsymbol{\lambda}_artheta$	$oldsymbol{\lambda}_{arphi}$	$ig  oldsymbol{\lambda}_u$	$ig  oldsymbol{\lambda_v}$
-0.177549478	0.0	0.0	0.060302417	-0.230424016
•				
$oldsymbol{\lambda}_w$	$oldsymbol{\lambda}_m$	$t_1$	$\mid  t_f$	

**Table 5.2:** Initial conditions of the adjoint variables for the first manoeuvre, including switching and final time

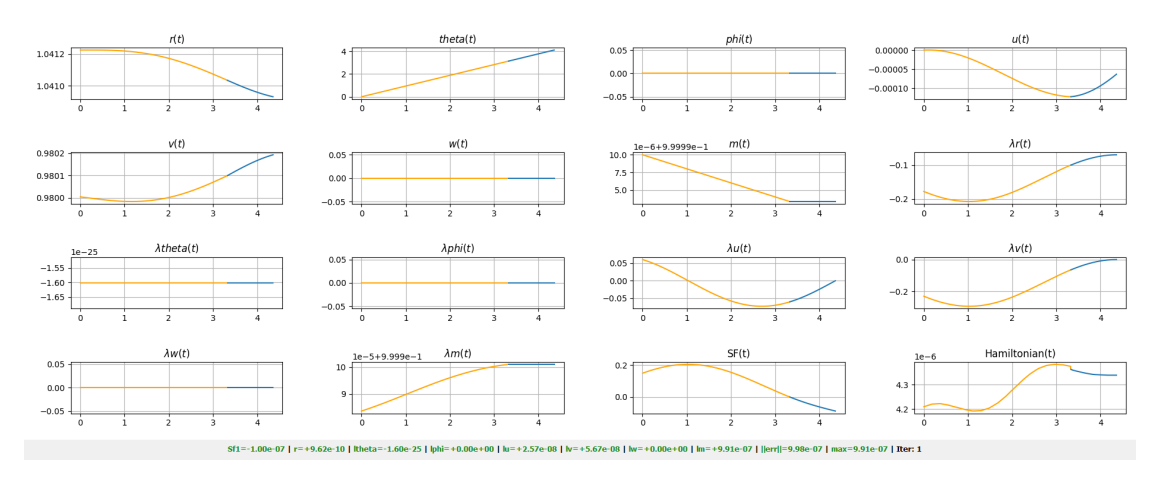


Figure 5.2: First manoeuvre

The plots in Figure 5.2 show how the orbital radius decreases progressively, while the tangential component of the velocity v tends to increase. The radial component u assumes a non-zero value, highlighting the transition of the orbit from circular to elliptical. The mass of the satellite decreases linearly due to propellant consumption, while the added variables  $\lambda_{\vartheta}$ ,  $\lambda_{\varphi}$ ,  $\lambda_{u}$ ,  $\lambda_{v}$ ,  $\lambda_{w}$  tend to zero, as required by the BCs shown in Table 5.3. Constraints were not imposed on the speed control components, but the corresponding added variables  $\lambda_{u}$ ,  $\lambda_{v}$  and  $\lambda_{w}$  were set to zero. Since the goal of this manoeuvre is to descend towards the surface and not to maintain a stable orbit, circularising the trajectory at the end of the manoeuvre would only result in an unnecessary increase in propellant consumption, without any real advantage, as well as slowing down the descent phase. Table 5.4 summarises the final state of the manoeuvre.

$m{r}$	$oldsymbol{\lambda}_{artheta}$	$\lambda_{arphi}$	$oldsymbol{\lambda}_u$	$oldsymbol{\lambda}_v$	$\lambda_w$	$\lambda_m$
1.0409305064782097	0.0	0.0	0.0	0.0	0.0	1.0

**Table 5.3:** Boundary conditions for the first manoeuvre

r	artheta	arphi	$oldsymbol{u}$
1.040930507441	4.103364763160	0.0	-6.309391661016e-05
21	$\boldsymbol{w}$	$m{m}$	
U	$\boldsymbol{w}$	116	

**Table 5.4:** Final state for the first manoeuvre

The errors on the boundary conditions (BCs) are visible in Figure 5.2 and are reported in detail in Table 5.5. It can be seen that all values are of the order of  $10^{-7}$ – $10^{-8}$ , fully compatible with the numerical tolerance adopted. In particular, the errors relating to  $\lambda_{\varphi}$  and  $\lambda_{w}$  are zero, while for the remaining variables the deviations are negligible. The calculated error norm is equal to  $9.98 \times 10^{-7}$ , which is lower than the convergence threshold set at  $10^{-6}$ , thus satisfying the required criterion. We can therefore conclude that the boundary conditions are respected with good accuracy and that the numerical solution obtained is consistent.

Figure 5.3 shows the trend of the dimensionless radius as a function of time, representing the propagation phase following the first manoeuvre. In this phase, the orbit is allowed to evolve freely for two orbital periods, corresponding to  $t_{\rm dim} = 13.345$ , equal to approximately 3.56 h. In this phase, no thrust is applied and the added variables are set to zero; consequently, the motion is governed solely by gravitational dynamics and interaction with atmospheric resistance.

$\Delta_{SI}$	Ţ.	$\Delta_r$	$\Delta_{\lambda_\vartheta}$	$\Delta_{\lambda_{arphi}}$	$ig  \Delta_{\lambda_u}$
$-1.0 \times$	$10^{-7}$	$9.62 \times 10^{-10}$	$-1.6 \times 10^{-25}$	0.0	$2.57 \times 10^{-8}$
$\Delta_{\lambda_i}$	,	$\Delta_{\lambda_w}$	$\Delta_{\lambda_m}$	err	$max_{err}$
$\overline{5.67 \times 1}$	$10^{-8}$	0.0	$9.91 \times 10^{-7}$	$9.98 \times 10^{-7}$	$9.91 \times 10^{-7}$

Table 5.5: Error on the BCs for the first manoeuvre

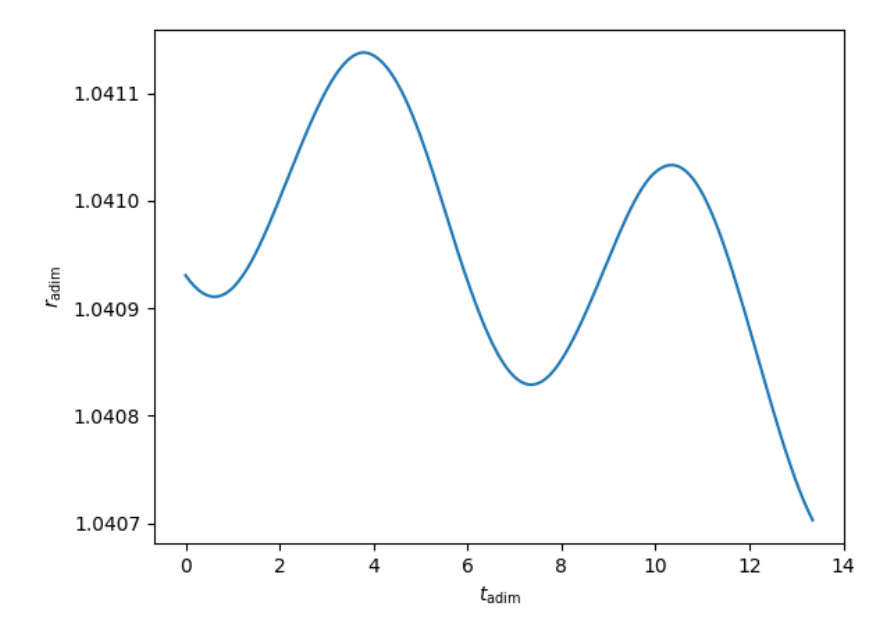


Figure 5.3: First propagation

The initial conditions of the second manoeuvre are shown in Table 5.6, while Table 5.7 summarises the status of the added variables and the characteristic switching and final times.

r	$\vartheta$	arphi	$oldsymbol{u}$
1.040702805556	16.66923321307	0.0	-8.467043918379e-05
$oldsymbol{v}$	$oldsymbol{w}$	m	
0.980305234032	0.0	0.999993381948	

Table 5.6: Initial state for the second manoeuvre

Figure 5.4 shows the evolution of the state variables during the second manoeuvre. Compared to the first, the variation in orbital radius is more pronounced. The

$oldsymbol{\lambda}_r$	$oldsymbol{\lambda}_artheta$	$\boldsymbol{\lambda}_{\varphi}$	$oldsymbol{\lambda}_u$	$oldsymbol{\lambda}_v$
-0.086225385	0.0	0.0	0.047594221	-0.087383016
$oldsymbol{\lambda}_w$	$oldsymbol{\lambda}_m$	$oldsymbol{t_1}$	$oldsymbol{t_f}$	
0.0	0.999987268	3.650506822	5.09120896	

**Table 5.7:** Initial conditions of the adjoint variables for the second manoeuvre, including switching and final time

elliptical nature of the orbit is also more clearly evident: the radius initially decreases, then increases slightly before decreasing again, thus following the profile required by the manoeuvre. The angle  $\vartheta$  increases to about 21.5 rad, confirming the progression of motion along the orbit, while the mass of the satellite continues to decrease in line with the consumption of propellant by the ion thruster. The boundary conditions, shown in Table 5.8, are respected with good accuracy, as can be seen in Table 5.9.

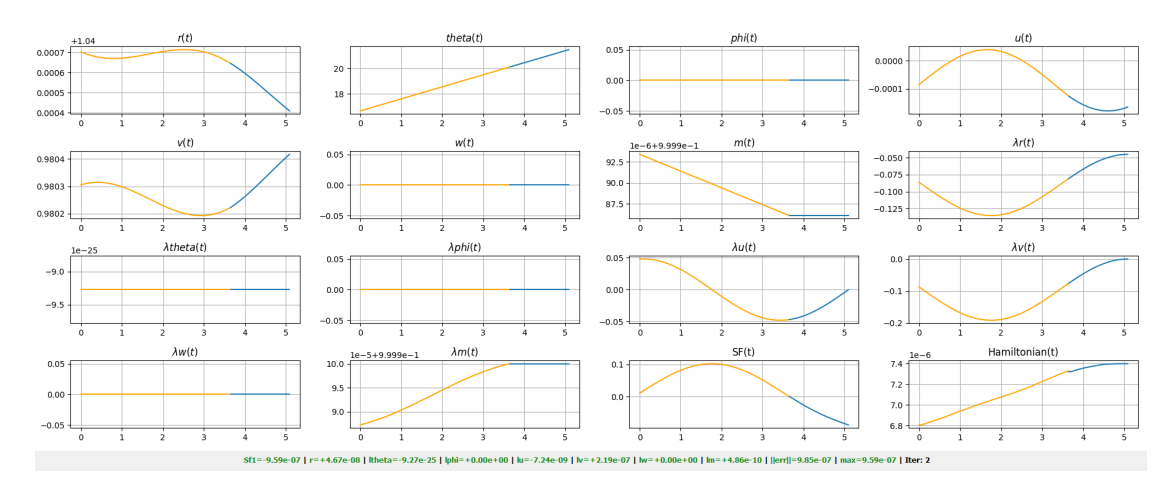


Figure 5.4: Second manoeuvre

$m{r}$	$oldsymbol{\lambda}_{artheta}$	$ig _{oldsymbol{\lambda}_arphi}$	$oldsymbol{\lambda}_u$	$oldsymbol{\lambda}_v$	$\lambda_w$	$\lambda_m$
1.0404089667482805	0.0	0.0	0.0	0.0	0.0	1.0

**Table 5.8:** Boundary conditions for the second manoeuvre

The final state of the second manoeuvre is shown in Table 5.10. Figure 5.5 shows the subsequent free propagation phase, during which a further lowering of the orbit and a more pronounced effect of atmospheric drag are observed, contributing to the progressive orbital decay. The propagation time is similar to that of the first

$\Delta_{SF}$	$igstar{\Delta_r}$	$ig  \Delta_{\lambda_artheta}$	$\Delta_{\lambda_{arphi}}$	$ig \Delta_{\lambda_u}$
$-9.59 \times 10^{-7}$	$4.67 \times 10^{-8}$	$-9.27 \times 10^{-25}$	0.0	$-7.24 \times 10^{-9}$
$\Delta_{\lambda_v}$	$\Delta_{\lambda_w}$	$\Delta_{\lambda_m}$	err	$max_{err}$
$-2.10 \times 10^{-7}$	0.0	$1.96 \times 10^{-10}$	$0.85 \times 10^{-7}$	$0.50 \times 10^{-7}$

**Table 5.9:** Error on the BCs for the second manoeuvre

phase, with a duration of approximately  $t_{\text{adim}} = 13.335$ .

r	artheta	arphi	$oldsymbol{u}$
1.040408388311	21.465057278128	0.0	-0.000164185438
$oldsymbol{v}$	$oldsymbol{w}$	m	
0.980418158085	0.0	0.999986109215	

Table 5.10: Final state for the second manoeuvre

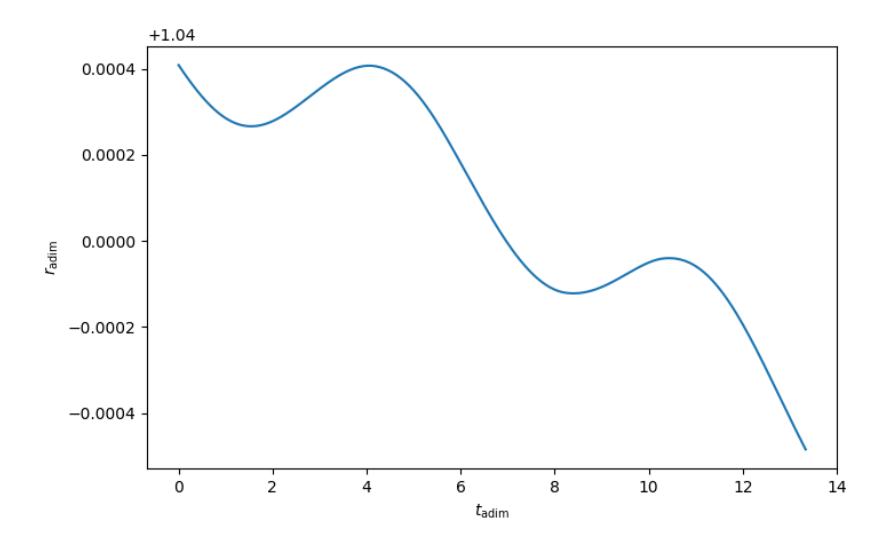


Figure 5.5: Second propagation

The initial conditions of the third manoeuvre are shown in Table 5.11, while Table 5.12 summarises the status of the added variables and the characteristic switching and final times.

r	$\vartheta$	arphi	$oldsymbol{u}$
1.03951532820759	34.037211778988	0.0	-0.0002096030794
$oldsymbol{v}$	$oldsymbol{w}$	m	
0.9808408014357	0.0	0.9999861092149	

Table 5.11: Initial state for the third manoeuvre

$\lambda_r$	$oldsymbol{\lambda}_artheta$	$\boldsymbol{\lambda}_{\varphi}$	$oldsymbol{\lambda}_u$	$oldsymbol{\lambda}_v$
-0.079162407	0.0	0.0	0.04385899	-0.079615017
$oldsymbol{\lambda_w}$	$oldsymbol{\lambda}_m$	$oldsymbol{t_1}$	$t_f$	
0.0	0.999988443	3.560358189	5.09120896	

**Table 5.12:** Initial conditions of the adjoint variables for the third manoeuvre, including switching and final time

The third manoeuvre, shown in Figure 5.6 with the ion thruster, marks the final phase of electric propulsion use. In this phase, orbital decay becomes more evident: the orbital radius is further reduced and the radial component of the velocity takes on more marked negative values, confirming the progressive transition towards increasingly elliptical orbits.

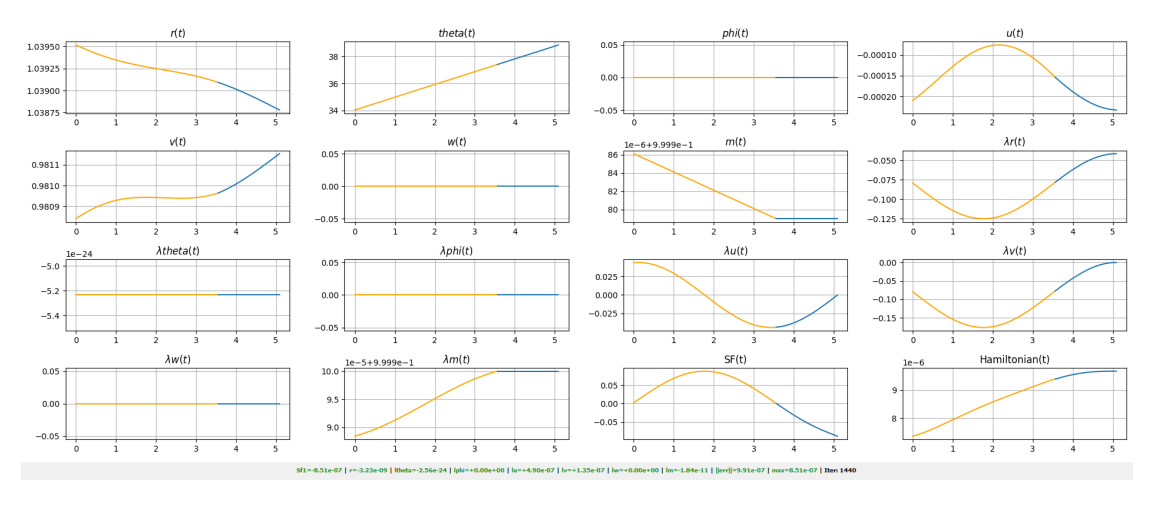


Figure 5.6: Third manoeuvre

The boundary conditions, shown in Table 5.13, are satisfied and the errors on the boundary conditions, summarised in Table 5.15, are all below the set convergence threshold. The final state of the manoeuvre is shown in Table 5.14.

					$\lambda_w$	
1.0387791680191292	0.0	0.0	0.0	0.0	0.0	1.0

**Table 5.13:** Boundary conditions for the third manoeuvre

$m{r}$	$\vartheta$	arphi	$oldsymbol{u}$
1.0387791572254	38.843213223712	0.0	-0.000232451706
$oldsymbol{v}$	$oldsymbol{w}$	$m{m}$	
0.9811542594848	0.0	0.999979016080	

**Table 5.14:** Final state for the third manoeuvre

$\Delta_{SF}$	$\Delta_r$	$\Delta_{\lambda_artheta}$	$\Delta_{\lambda_{\varphi}}$	$\Delta_{\lambda_u}$
$-8.51 \times 10^{-7}$	$-3.23 \times 10^{-9}$	$-2.56 \times 10^{-24}$	0.0	$4.9 \times 10^{-7}$
$\boldsymbol{\Delta}_{\lambda_v}$	$\Delta_{\lambda_w}$	$\Delta_{\lambda_m}$	err	$max_{err}$

Table 5.15: Error on the BCs for the third manoeuvre

This manoeuvre represents the last use of the ion thruster before the vehicle's deceleration is entrusted to interaction with the Martian atmosphere. The subsequent free propagation, illustrated in Figure 5.7, shows further orbital decay, in which aerodynamic drag becomes the dominant phenomenon and prepares the conditions necessary for the parachute to open in the next phase of the mission. In this case, the propagation time is greater than two orbital periods, with a value of  $t_{\rm adim} = 14.267$ , chosen to allow the vehicle to reach the predetermined altitude for the parachute to open.

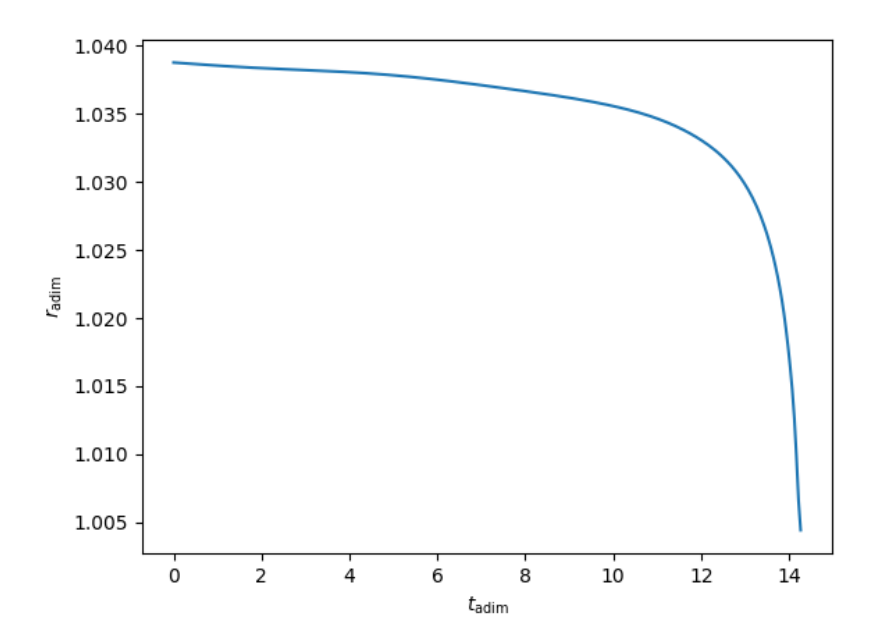


Figure 5.7: Third propagation

#### 5.2 Parachute

Once the predetermined altitude of 15 km is reached, the parachute is activated (Figure 5.8). The initial state of this phase is shown in Table 5.16. With the opening of the parachute, the surface area exposed to the atmosphere increases to  $200 \ m^2$ , while the aerodynamic drag coefficient  $C_D$  is reduced from 2.2, valid in the previous phase, to 1.7. The deployment sequence, lasting approximately 2 minutes, causes a sharp reduction in speed, as shown by the final state of the satellite reported in Table 5.17, coinciding with the initial conditions of the last manoeuvre. In this phase, the trajectory is strongly influenced by atmospheric drag, which allows a significant amount of the vehicle's kinetic energy to be rapidly dissipated.

$m{r}$	artheta	arphi	$oldsymbol{u}$
1.0044159119018	52.297915646224	0.0	-0.0463679099419
$oldsymbol{v}$	$oldsymbol{w}$	$m{m}$	

Table 5.16: Initial state for the trajectory with parachute

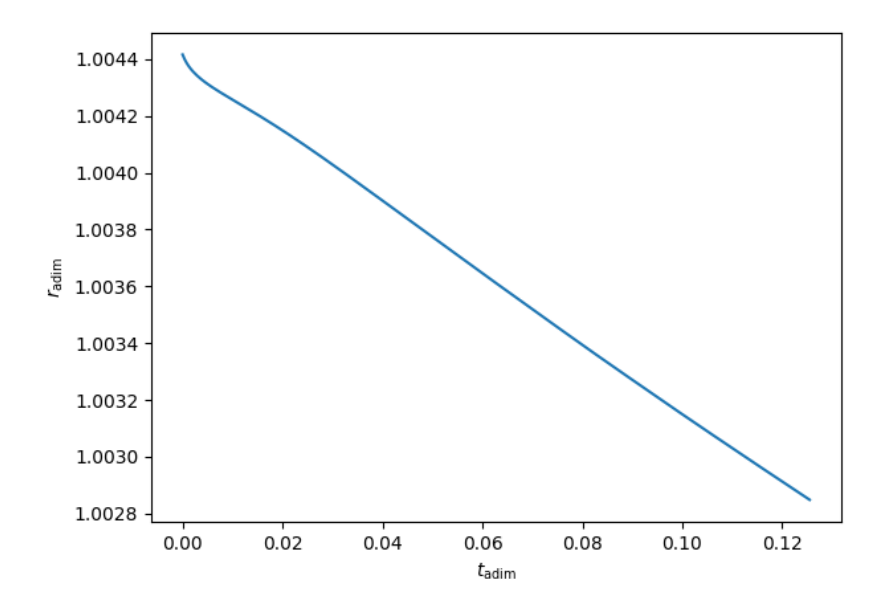


Figure 5.8: Trajectory with open parachute

#### 5.3 Chemical Thrusters

However, unlike Section 5.1, which used an electric thruster, in this phase with the chemical thruster, the manoeuvre is divided into two distinct stages: an initial coasting phase, during which the engine remains off, followed by the ignition of the thruster, which is necessary to slow down the vehicle and ensure a controlled and precise landing.

$m{r}$	artheta	arphi	$oldsymbol{u}$
1.0028486927687	52.306989827031	0.0	-0.0116797819309
$oldsymbol{v}$	$oldsymbol{w}$	m	
0.0679949421274	0.0	0.999979016080	

Table 5.17: Initial state for the last manoeuvre

$oldsymbol{\lambda}_r$	$oldsymbol{\lambda}_artheta$	$\boldsymbol{\lambda}_{\varphi}$	$oldsymbol{\lambda}_u$	$oldsymbol{\lambda}_v$
-0.347800000	0.0	0.0	0.001396000	-0.736543560
$oldsymbol{\lambda}_w$	$oldsymbol{\lambda}_m$	$oldsymbol{t_1}$	$oldsymbol{t_f}$	
0.0	0.937903811	0.256839800	0.257424320	

**Table 5.18:** Initial conditions of the adjoint variables for the last manoeuvre, including switching and final time

As shown in the plots in Figure 5.9 and reported in more detail in Table 5.20, the objective of a safe and controlled landing was achieved starting from the initial conditions indicated in Table 5.18. The final radius assumed the value r = 1.000000102, corresponding to approximately 34 cm from the planet's surface. The velocities are close to zero: in particular, the radial component is equal to  $u = 7.4 \times 10^{-7}$ , m/s, while the tangential velocity to the surface is equal to  $v = 2.55 \times 10^{-5}$ , m/s. The total duration of the manoeuvre, including the coasting phase and the subsequent ignition of the chemical propulsion system, is approximately 4 minutes, of which the last 10 seconds were characterised by the ignition of the engine to ensure a controlled landing.

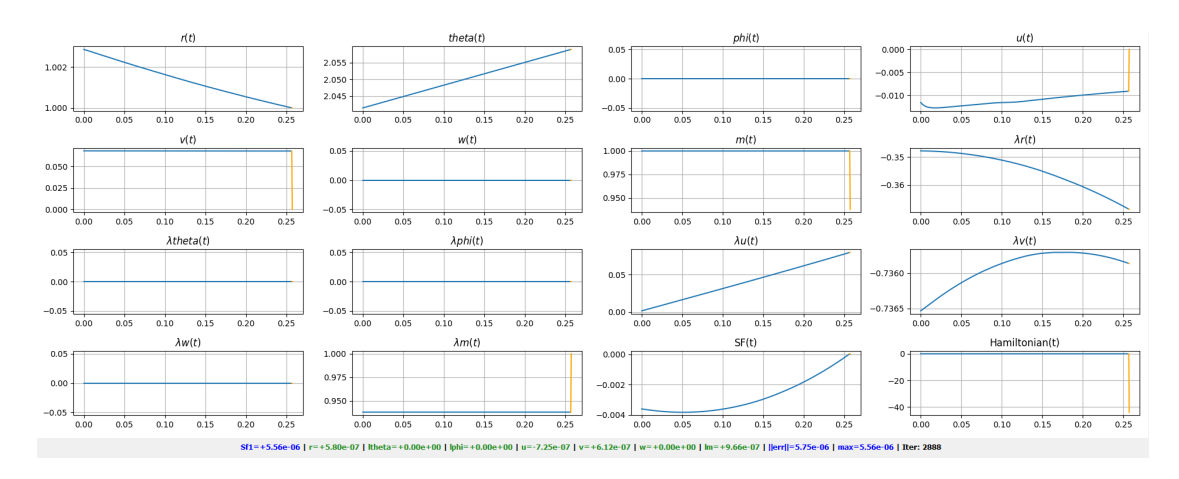


Figure 5.9: Last manoeuvre

r	$oldsymbol{\lambda}_{artheta}$	$oldsymbol{\lambda}_{arphi}$	u	v	w	$\lambda_m$
1.0	0.0	0.0	0.0	0.0	0.0	1.0

Table 5.19: Boundary conditions for the last manoeuvre

r	$\boldsymbol{\vartheta}$	$\varphi$	$oldsymbol{u}$	$oldsymbol{v}$	w	m
1.000000102	2.05893898	0.0	0.000000058	0.000002116	0.0	0.937886087

Table 5.20: Final state

#### 5.4 Overview

This chapter presents the numerical results of the Mars descent mission, obtained through simulations in Python. After an initial phase of three ion thruster manoeuvres, alternating with free propagation, the vehicle's orbit gradually decayed to altitudes where atmospheric drag became predominant.

Once an altitude of 15 km was reached, the parachute was deployed, allowing for rapid dissipation of kinetic energy and a significant slowdown in trajectory. In the final phase, the ignition of the chemical thruster ensured a controlled and safe landing, with negligible residual velocity.

To provide an overview, Figures 5.10 and 5.11 show the entire descent profile and a detail of the final phase, respectively, highlighting the different phases: the elliptical orbits due to ion manoeuvres, the abrupt change in trajectory when the parachute opened, and the final deceleration imposed by the chemical thruster. These figures allow us to appreciate the consistency of the descent strategy and the correct sequence of manoeuvres that led to a safe landing.

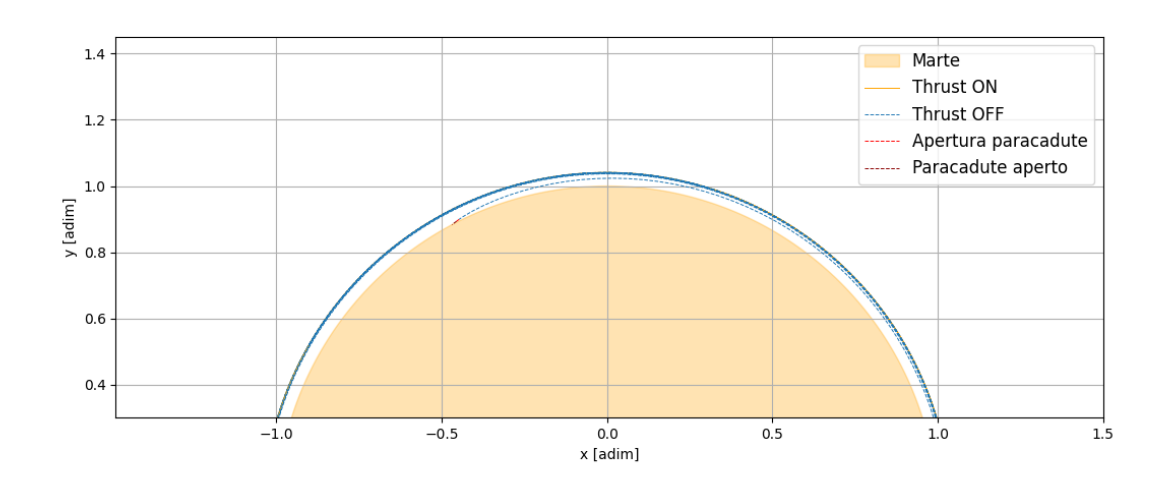


Figure 5.10: Complete trajectory

In addition to considerations regarding the dynamic evolution of the mission, it

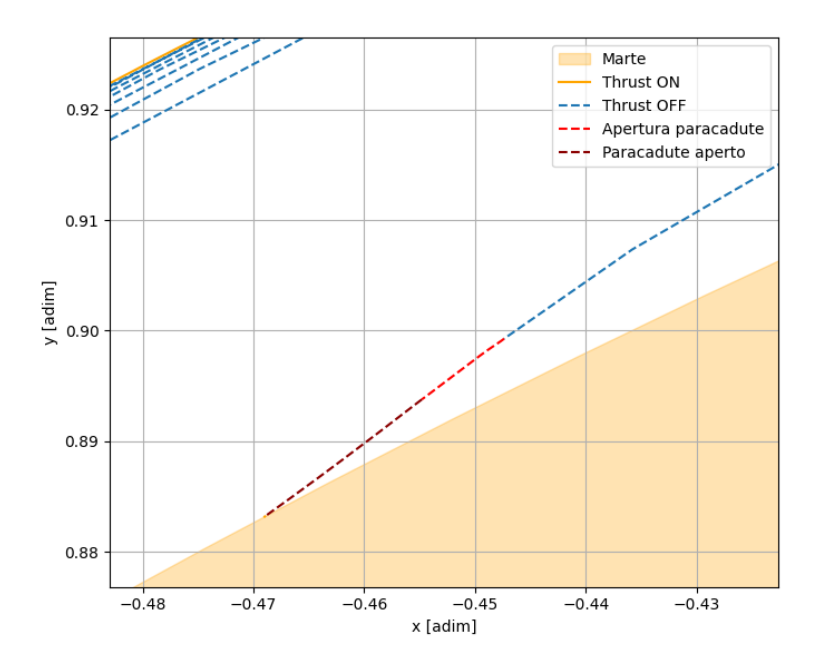


Figure 5.11: Zoom in on the final landing phase

is also useful to analyse the overall mass consumption.

Starting from an initial dimensionless mass of 1, at the end of the last manoeuvre with the ion propulsion system, the residual mass is m = 0.99997902, while at the end of the mission it is m = 0.93788609. The overall consumption is therefore  $\Delta_m = 0.0621$ , corresponding to approximately 6.2% of the initial mass.

The part attributable to the electric phase is extremely small: only  $\Delta_{m_{\rm ions}} \approx 2.1 \times 10^{-5}$ , equal to 0.002%, while the chemical phase involved a consumption of  $\Delta_{m_{\rm chem}} \approx 0.0621$ , equivalent to almost the entire amount. Assuming an initial mass of 600 kg, this corresponds to approximately 12.6 g of propellant used by the ion thruster and 37.3 kg consumed by the chemical thruster, for a total of approximately 37.31 kg.

This result highlights the complementary nature of the two propulsion systems: on the one hand, the ion thruster, which is extremely efficient in terms of mass consumption but limited in terms of thrust; on the other hand, the chemical thruster, which is capable of providing the thrust necessary to ensure a controlled landing, but at a significantly higher cost in terms of mass.

Finally, it should be noted that, without the manoeuvres performed with the electric propulsion system, the time required for orbital decay and subsequent landing would have been approximately one hour longer. This result confirms that the use of the ion propulsion system, while requiring negligible amounts of propellant, contributed significantly to the temporal efficiency of the mission.

## Chapter 6

### Conclusions

This thesis addresses the problem of controlled descent on Mars from a circular orbit at an altitude of 140 km. The objective was to develop and validate, using a numerical code implemented in Python, a safe and controlled landing strategy based on a combination of ion thrusters, parachutes and chemical propulsion.

#### 6.1 Key strengths

A first important aspect concerns the adoption of a dimensionless approach, which simplified the numerical analysis by avoiding the management of large quantities and allowing greater clarity in reading the results. Furthermore, the use of the indirect method in optimal control theory made it possible to obtain good quality approximate solutions with a low computational cost, demonstrating the effectiveness of this technique in addressing complex mission analysis problems. Finally, the code developed in Python proved to be flexible and easily adaptable to scenarios other than the one analysed in this thesis. With appropriate changes to the initial parameters, it could in fact be applied to missions of a different nature, such as the removal of space debris or the deployment of satellite constellations in multiple orbits.

#### 6.2 Limitations

Alongside its strengths, it is necessary to highlight the main limitations of the model adopted. The atmospheric model has been treated in a simplified form, considering aerodynamic resistance as the only disturbance. Other effects that would have a significant impact on a real scenario, such as the term  $J_2$ , solar radiation, the influence of third bodies or eclipses, which would make it impossible to use the electric propulsion system continuously in the absence of solar energy, have not

been included. Although these approximations do not compromise the qualitative validity of the results, they do reduce their accuracy with respect to an operational application.

#### 6.3 Next Steps in the Research

Starting from the identified limitations, several future developments are possible. A first step is to integrate additional perturbations into the model, including the contribution of  $J_2$ , eclipses, solar radiation, and the effect of third bodies, already presented in the theoretical part of the thesis. A second possible extension concerns the definition of more complex missions, for example starting from higher orbits, not immediately subject to atmospheric resistance, or considering a complete mission that includes departure from Earth, a lunar passage similar to the Artemis programme, interplanetary transfer and final landing. Finally, a further interesting development concerns the graphical interface created to support the code. In the future, it could be made more flexible and interactive, allowing direct selection of which perturbations to consider, the reference system to be adopted and the planet around which to conduct the mission, thus expanding the database of available atmospheres and parameters. In this way, the GUI could become a comprehensive tool for simulating complex space scenarios.

The work carried out has demonstrated the feasibility of the proposed strategy for controlled descent on Mars and the validity of the model implemented. The results obtained confirm the effectiveness of the methodology adopted and provide a solid basis for extending the analysis to future missions of increasing complexity, in line with the prospects for space exploration that will characterise the coming decades.

## Appendix A

## **Rotational Matrices**

$$L_{SEZ \to IJK} = R_3(\vartheta)^T R_2(\varphi)^T = \begin{bmatrix} \cos \vartheta & -\sin \vartheta & 0 \\ \sin \vartheta & \cos \vartheta & 0 \\ 0 & 0 & 1 \end{bmatrix} \begin{bmatrix} \cos \varphi & 0 & -\sin \varphi \\ 0 & 1 & 0 \\ \sin \varphi & 0 & \cos \varphi \end{bmatrix}$$

$$= \begin{bmatrix} \cos \varphi \cos \vartheta & -\sin \vartheta & -\sin \varphi \cos \vartheta \\ \cos \varphi \sin \vartheta & \cos \vartheta & -\sin \varphi \sin \vartheta \\ \sin \varphi & 0 & \cos \varphi \end{bmatrix}$$
(A.2)

## Appendix B

# Spherical Unit Vectors

$$\hat{e}_r = \begin{bmatrix} \cos \varphi & \cos \vartheta \\ \sin \varphi & \cos \vartheta \\ \sin \vartheta \end{bmatrix}$$
 (B.1a)

$$\hat{e}_{\vartheta} = \frac{1}{\cos \varphi} \begin{bmatrix} -\cos \varphi & \sin \vartheta \\ \cos \varphi & \cos \vartheta \end{bmatrix}$$
 (B.1b)

$$\hat{e}_{\varphi} = \begin{bmatrix} -\sin\varphi \cos\vartheta \\ -\sin\varphi \sin\vartheta \\ \cos\varphi \end{bmatrix}$$
 (B.1c)

$$\hat{e}_{\varphi} = \begin{bmatrix} -\sin\varphi \cos\vartheta \\ -\sin\varphi \sin\vartheta \\ \cos\varphi \end{bmatrix} \tag{B.1c}$$

$$\dot{\hat{e}}_{r} = \begin{bmatrix} -\dot{\varphi}\sin\varphi\cos\vartheta - \dot{\vartheta}\cos\varphi\sin\vartheta \\ -\dot{\varphi}\sin\varphi\sin\vartheta - \dot{\vartheta}\cos\varphi\cos\vartheta \end{bmatrix} = \dot{\vartheta}\cos\varphi\,\hat{e}_{\vartheta} + \dot{\varphi}\,\hat{e}_{\varphi} \tag{B.1d}$$

$$\dot{\varphi}\cos\varphi$$

$$\dot{\hat{e}}_{\vartheta} = \begin{bmatrix} -\dot{\vartheta}\cos\vartheta \\ -\dot{\vartheta}\sin\vartheta \\ 0 \end{bmatrix} = -\dot{\vartheta}\cos\varphi\,\hat{e}_r + \dot{\vartheta}\sin\varphi\,\hat{e}_{\varphi}$$
 (B.1e)

$$\dot{\hat{e}}_{\varphi} = \begin{bmatrix} -\dot{\varphi}\cos\varphi\cos\vartheta + \dot{\vartheta}\sin\varphi\sin\vartheta \\ -\dot{\varphi}\cos\varphi\sin\vartheta - \dot{\vartheta}\sin\varphi\cos\vartheta \end{bmatrix} = -\dot{\varphi}\,\hat{e}_{r} - \dot{\vartheta}\sin\varphi\,\hat{e}_{\vartheta} \qquad (B.1f)$$

$$\dot{\varphi}\sin\varphi$$

## Appendix C

# Euler-Lagrange equations for the adjoint variables

$$\dot{\vec{\lambda}} = -\frac{\partial \mathcal{H}}{\partial \vec{x}} \tag{C.1}$$

$$\dot{\lambda}_{r} = \frac{1}{r^{2}} \left[ \lambda_{\vartheta} \frac{v}{\cos \varphi} + \lambda_{\varphi} w + \lambda_{u} \left( -\frac{2u}{r} + v^{2} + w^{2} \right) + \lambda_{v} (-uv + vw \tan \varphi) \right. \\ + \left. \lambda_{w} (-uv - v^{2} \tan \varphi) \right] - \lambda_{u} \frac{\partial (a_{p})_{u}}{\partial r} - \lambda_{v} \frac{\partial (a_{p})_{v}}{\partial r} - \lambda_{w} \frac{\partial (a_{p})_{w}}{\partial r} - S_{F} \frac{\partial T}{\partial r} \quad (C.2a)$$

$$\dot{\lambda}_{\vartheta} = -\lambda_{u} \frac{\partial (a_{p})_{u}}{\partial \vartheta} - \lambda_{v} \frac{\partial (a_{p})_{v}}{\partial \vartheta} - \lambda_{w} \frac{\partial (a_{p})_{w}}{\partial \vartheta} + S_{F} \frac{\partial T}{\partial \vartheta}$$
(C.2b)

$$\dot{\lambda}_{\varphi} = \frac{1}{r \cos^2 \varphi} \left( -\lambda_{\vartheta} v \sin \varphi - \lambda_u v w + \lambda_v w + \lambda_w v^2 \right)$$

$$-\lambda_u \frac{\partial (a_p)_u}{\partial \varphi} - \lambda_v \frac{\partial (a_p)_v}{\partial \varphi} - \lambda_w \frac{\partial (a_p)_w}{\partial \varphi} + S_F \frac{\partial T}{\partial \varphi}$$
(C.2c)

$$\dot{\lambda}_u = \frac{1}{r} \left( -\lambda_r r + \lambda_u v + \lambda_w w \right) \tag{C.2d}$$

$$\dot{\lambda}_v = \frac{1}{r} \left[ -\frac{\lambda_{\vartheta}}{\cos \varphi} - 2\lambda_u v + \lambda_u (u - w \tan \varphi) + 2\lambda_w v \tan \varphi \right]$$
 (C.2e)

$$\dot{\lambda}_w = \frac{1}{r} \left( -\lambda_\varphi - 2\lambda_u w - \lambda_v v \tan \varphi + \lambda_w u \right) \tag{C.2f}$$

$$\dot{\lambda}_m = \frac{T}{m^2} \lambda_V - \lambda_u \frac{\partial (a_p)_u}{\partial m} - \lambda_v \frac{\partial (a_p)_v}{\partial m} - \lambda_w \frac{\partial (a_p)_w}{\partial m}$$
 (C.2g)

## Bibliography

- [1] Cicerone. De Legibus. Libro I, par. 5. 45 BCE (cit. on p. 1).
- [2] François Hartog. Il mito di Erodoto. Einaudi, 1988 (cit. on p. 1).
- [3] Konstantin Eduardovich Tsiolkovsky. The Exploration of Cosmic Space by Means of Reaction Devices. Russian. Originally published in Russian: Issledovanie mirovykh prostranstv reaktivnymi priborami. 1903 (cit. on p. 2).
- [4] Lorenzo Casalino. Space Propulsion. Slide del corso di Propulsione Spaziale, Politecnico di Torino. Materiale didattico. 2024 (cit. on p. 3).
- [5] John T. Betts. Practical Methods for Optimal Control and Estimation Using Nonlinear Programming. Advances in Design and Control. 2010. ISBN: 978-0-89871-688-7. DOI: 10.1137/1.9780898718577 (cit. on p. 4).
- [6] A. M. Dwyer Cianciolo H. L. Justh and J. Hoffman. Mars Global Reference Atmospheric Model (Mars-GRAM): User Guide. Tech. rep. NASA/TM-20210023957. Marshall Space Flight Center Huntsville, Alabama 35812: National Aeronautics and Space Administration, Nov. 2021 (cit. on pp. 4, 31).
- [7] Isaac Newton. *Philosophiæ Naturalis Principia Mathematica*. Opera originale in cui Newton enuncia le leggi del moto e la legge di gravitazione universale. Londini: Jussu Societatis Regiæ ac Typis Josephi Streater, 1687 (cit. on p. 7).
- [8] Luigi Mascolo. «Low-Thrust Optimal Escape Trajectories from Lagrangian Points and Quasi-Periodic Orbits in a High-Fidelity Model». PhD thesis. Torino: Politecnico di Torino, 2023. URL: https://iris.polito.it/handle/11583/2976595 (cit. on pp. 18, 20, 49).
- [9] Manuela Battipede. *Meccanica del Volo Spaziale*. Slide del corso di Propulsione Spaziale, Politecnico di Torino. Materiale didattico. 2024 (cit. on pp. 18, 20).
- [10] David A. Vallado. Fundamentals of Astrodynamics and Applications. 4th. Vol. 12. Space Technology Library. Microcosm Press / Springer, 2013. ISBN: 978-1881883180 (cit. on p. 25).
- [11] Pedro Ramon Escobal. Methods of Orbit Determination. Originally published in 1965 by John Wiley & Sons, New York. Malabar, FL: Krieger Publishing Company, 1985 (cit. on p. 25).

- [12] R. M. Haberle, C. B. Leovy, and J. B. Pollack. «Some Effects of Global Dust Storms on the Atmospheric Circulation of Mars». In: *Icarus* 50 (1982), pp. 322–367 (cit. on p. 37).
- [13] Z. J. Ye, M. Segal, and R. A. Pielke. «A comparative study of daytime thermally induced upslope flow on Mars and Earth». In: *Journal of the Atmospheric Sciences* 47.5 (1990), pp. 612–628 (cit. on p. 37).
- [14] F. Forget, F. Hourdin, R. Fournier, C. Hourdin, O. Talagrand, M. Collins, S. R. Lewis, P. L. Read, and J.-P. Huot. «Improved general circulation models of the Martian atmosphere from the surface to above 80 km». In: *Journal of Geophysical Research: Planets* 104.E10 (1999), pp. 24155–24176 (cit. on p. 40).
- [15] Guido Colasurdo. «Optimal Finite-Thrust Spacecraft Trajectories». In: *Proceedings of the Astrodynamics Conference*. 1992. DOI: 10.2514/6.1992-4510 (cit. on p. 45).
- [16] Guido Colasurdo and Dario Pastrone. «Indirect Optimization Method for Impulsive Transfers». In: Proceedings of the Astrodynamics Conference. 1994. DOI: 10.2514/6.1994-3762 (cit. on p. 45).
- [17] Lorenzo Casalino, Guido Colasurdo, and Dario Pastrone. «Optimal Three-Dimensional Trajectories for Manned Mars Missions». In: Proceedings of the Astrodynamics Conference. 1996. DOI: 10.2514/6.1996-3612 (cit. on p. 45).
- [18] Lorenzo Casalino, Guido Colasurdo, and Dario Pastrone. «Indirect Approach for Minimum-Fuel Aeroassisted Transfers». In: *Proceedings of the Astrodynamics Conference*. 1996, pp. 192–200. DOI: 10.2514/6.1996-3592 (cit. on p. 45).
- [19] Lorenzo Casalino, Guido Colasurdo, and Dario Pastrone. «Optimization Procedure for Preliminary Design of Opposition-Class Mars Missions». In: *Journal of Guidance, Control, and Dynamics* 21.1 (1998), pp. 134–140. DOI: 10.2514/2.4209 (cit. on p. 45).
- [20] J. P. McDanell and W. F. Powers. «Necessary Conditions Joining Optimal Singular and Nonsingular Subarcs». In: *SIAM Journal on Control* 9.2 (1971), pp. 161–173. DOI: 10.1137/0309014 (cit. on p. 48).